

First-Principles Study of Thermoelectric Effect in Two-dimensional Ferromagnet

メタデータ	言語: eng 出版者: 公開日: 2021-03-17 キーワード (Ja): キーワード (En): 作成者: メールアドレス: 所属:
URL	http://hdl.handle.net/2297/00061347

This work is licensed under a Creative Commons Attribution-NonCommercial-ShareAlike 3.0 International License.



Dissertation

First-Principles Study of Thermoelectric Effect in Two-dimensional Ferromagnet

二次元強磁性体における熱電効果の第一原理的研究

Graduate School of
Natural Science & Technology
Kanazawa University

Division of Mathematical and Physical Sciences

Student ID: 1724012009

Name : Rifky Syariati

Chief Advisor : Prof. Fumiyuki ISHII

Date of Submission : 22 October 2020

First-Principles Study of Thermoelectric Effect in Two-dimensional Ferromagnet

(二次元強磁性体における熱電効果の第一原理的研究)

Rifky Syariati

Abstract

We implemented first-principles calculations to elucidate the anomalous Nernst effect (transverse thermoelectric effect) of the half-metallic FeCl_2 monolayer. We investigated its thermoelectric properties based on the semiclassical transport theory including the effect of Berry curvature. If we assumed 10 fs for the relaxation time, the carrier-doping generates a large anomalous Nernst effect which was approximately $6.65 \mu\text{V/K}$ at 100 K. The origin of this large magnitude comes from large Berry curvature at K-point of hexagonal Brillouin zone. These results indicate that two-dimensional ferromagnetic half-metallic materials can potentially be applied in thermoelectric devices.

Key words: First-principles calculation, two-dimensional magnetic materials, thermoelectric, anomalous Hall effect, anomalous Nernst effect

Acknowledgements

Throughout the writing of this dissertation, I have received a great deal of support and assistance. On this page, I wish to express my sincere gratitude to my supervisor, Prof. Fumiyuki Ishii, for his motivation, support, and guidance during my study. He has given me an opportunity and complete freedom to work on interesting research topics during the last three years. His insightful feedback pushed me to sharpen my thinking and brought my work to a higher level.

I am thankful to the Ministry of Education, Culture, Sports, Science and Technology (MEXT), Japan, and Kanazawa University, Japan, for financial support through the Global Human Resource (GHR) Development scholarship program.

I would like to acknowledge computational science research group members: Mr. Mizuta, Mr. Minami, Mr. Sawahata, Mr. Yamaguchi, Mr. Teguh, Mr. Manaf, Mrs. Monika, Mr. Yusuf, and Mrs. Aflah. I want to thank you for your patient support and for all of the opportunities that I was given to further my research. They provided me with the tools that I needed to choose the right direction and successfully complete my dissertation.

I would like to acknowledge my supervisor at Institute Teknologi Bandung (ITB), Prof. Khairurrijal for his support, encouragement, and motivation to get higher education abroad. Also, I would like to thank to my Indonesian friends, especially in Indonesia Student Association Ishikawa (PPI Ishikawa) and Indonesia-Ishikawa Moslem Family Association (KMI Ishikawa) for their valuable guidance throughout my studies.

Finally, my deep and sincere gratitude to my family for their continuous and unparalleled love, help, and support. I am grateful to my wife (Lilih Siti Solihat) and my children (Haisha Hanum Hanania and Ahnaf Auni Minha) for always being there for me. I am forever indebted to my parents for giving me the opportunities and experiences that have made me who I am. They selflessly encouraged me to explore new directions in life and seek my own destiny. This journey would not have been possible if not for them, and I dedicate this milestone to them.

Contents

1	Introduction	7
1.1	Motivation	7
1.2	An Overview of Anomalous Nernst Effect	8
1.3	Anomalous Nernst Effect Based in the 2D Magnetic Materials	9
1.4	The Purpose of This Study	10
1.5	Outline of Dissertation	10
2	Background: Basic Theory and Computational Methods	12
2.1	Density Functional Theory (DFT)	12
2.2	Norm Conserving Pseudo-potential and Pseudo-atomic Basis Orbitals	18
2.3	Non-collinear Density Functional Theory	20
2.4	Maximally Localized Wannier Functions	22
2.5	Octahedral Crystal Field Theory and Super Exchange Interaction	24
2.6	Thermoelectric Properties Based Anomalous Nernst Effect	27
2.7	Computational Scheme	29
3	Magnetic and Electronic Properties of 1T-FeCl₂ Monolayer	30
3.1	Atomic Structure of 1T-FeCl ₂ Monolayer	30
3.2	Magnetic Properties	31
3.3	Electronic Properties	33
4	Thermoelectric Properties of 1T-FeCl₂ Monolayer	36
4.1	Anomalous Nernst Coefficient	36
4.2	Anomalous Hall Conductivity	37
4.3	Band Contribution to Anomalous Hall Conductivity	40
5	Conclusion	42
5.1	Summary	42
5.2	Future Scope	43

List of Figures

1.1	The schematics of thermoelectric based (a) Seebeck effect and (b) anomalous Nernst effect	8
2.1	The schematics of Kohn-Sham equation self-consistent calculation. . .	17
2.2	The different of (a) single transition metal orbital energy and (b) when ligands approach the transition metal ion which forming octahedral structure	25
3.1	(a) Side and (b) top views of 1T-FeCl ₂ monolayer structure. Brown and green spheres indicate Fe and Cl atoms, respectively. Structural parameters of 1T-FeCl ₂ monolayer, namely, angle between Fe-Cl-Fe atoms, vertical distance of Cl-Cl atoms, and distance between Fe-Cl atom are represented by θ , d_{Cl-Cl} , d_{Fe-Cl} , respectively.	31
3.2	Configuration mode for (a) FM and (b) AFM spin arrangements . . .	32
3.3	The electronic structure of the ferromagnetic 1T-FeCl ₂ monolayer, which consists of spin polarized (a) band structure and (b) density of states where red and black lines indicate the majority and minority states, respectively, and (c) the projected density of states (PDOS) .	34
4.1	Chemical potential and temperature dependence of anomalous Nernst coefficient (ANC), N , at 50 K and 100 K on 1T-FeCl ₂ monolayer. . .	37
4.2	Chemical potential and temperature dependence of (a) pure Nernst coefficient, N_0 , and (b) pure Seebeck coefficient, S_0 , at 50 K and 100 K on 1T-FeCl ₂ monolayer.	38
4.3	Chemical potential and temperature dependence of (a) the AHC (σ_{xy}) and the (b) longitudinal electrical conductivity (σ_{xx}) with $\tau = 10$ fs at 0 K.	38
4.4	Chemical potential dependence of α_{xy} , and $\sigma_{xy}S_0$ at 100 K.	39
4.5	(a) Band structure with SOI, band decomposition in the chemical potential dependence of (b) σ_{xy} and (c) α_{xy} of 1T-FeCl ₂ monolayer. Red, blue, and green lines indicate the band contribution near Fermi level.	40

4.6	The chemical potential dependence of (a) Berry curvature summation at $\mu \sim 0.2$ eV, and (b) Berry curvature from band decomposition of 1T-FeCl ₂ monolayer. Red, blue, and green lines indicate the band contribution near Fermi level.	41
-----	---	----

List of Tables

3.1	The atomic and magnetic parameters of 1T-FeCl ₂ monolayer which consist of lattice constant a , the angle of Fe-Cl-Fe atoms θ , magnetic anisotropy energy (MAE) E_{MAE} , magnetic moment m , the different energy between FM and AFM E_{EX} , exchange splitting energy J , and Curie temperature T_c	33
4.1	Thermoelectric properties of 1T-FeCl ₂ monolayer without carrier doping calculated by constant relaxation time, $\tau = 10fs$	36
4.2	The peaks of N at chemical potential μ in the Figure 4.1a which is contributed by N_0 , θ_H , and S_0 at 100 K.	37
5.1	The 2D magnetic materials which experimentally discovered	43

Chapter 1

Introduction

1.1 Motivation

Nowadays, the demand for energy supplies increases especially for the Internet of Things (IoT). One of the possible energy sources for IoT is the waste heat. The waste heat can be found everywhere especially in inefficient primary energy and it can be an environmental pollutant. By recovering the waste heat, energy and environmental problems can be solved. One of the solutions which can recover the waste heat is thermoelectric devices.

Thermoelectric generation is a method to generate electricity from the heat. It is a clean conversion because it uses not only waste heat from such as motor vehicles, households, and factories but also heats from environmental heat sources. Thermoelectric generators are solid-state semiconductor devices that convert a temperature difference and heat flow into a useful DC power source. The basic building block of a thermoelectric generator is a thermocouple which is made up of one p-type semiconductor and one n-type semiconductor as shown in Fig. 1.1 (a). The semiconductors are connected serially by a metal strip. Thermoelectric generator semiconductor devices employ the Seebeck effect to generate a voltage. This generated voltage generates electrical current and produces useful power at a load.

The Seebeck effect is a direct energy conversion of heat into a voltage potential with the Peltier current. This effect is occurred due to the movement of charge carriers within the semiconductors. In doped n-type semiconductors, the charge carriers are electrons while the doped p-type semiconductors, charge carriers are holes. Charge carriers diffuse from the hot to the cold side of the semiconductor. This will create a voltage potential that proportional to the temperature difference across the semiconductor. However, there is a deficiency in Seebeck energy conversion. The Peltier heat current will convey heat sometimes which degrading the conversion efficiency. Because of that, the researchers try to resolve this problem

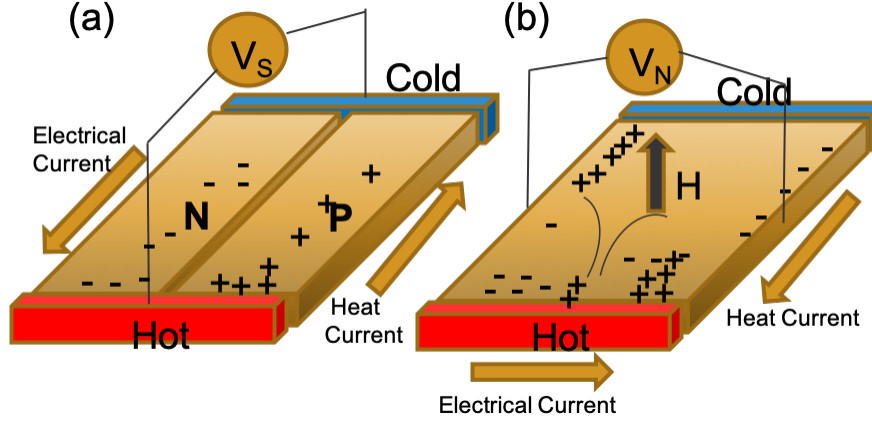


Figure 1.1: The schematics of thermoelectric based (a) Seebeck effect and (b) anomalous Nernst effect

by using the magnetic material which generating anomalous Nernst effect (ANE) in thermoelectric devices.

The anomalous Nernst effect (ANE) thermoelectric power generation attracts the researcher due to its flexible and simple structure and low generation cost in fabrication [1]. ANE offers for high flexibility degree in device design since when the temperature gradient is applied, the material length along the temperature gradient is not needed because the anomalous Nernst voltage increases with the transverse length normal to both the magnetization and the temperature gradient. Thus, thermoelectric devices based on the ANE can be adaptable with any heat source. So that, the materials such as thin films and two-dimensional (2D) materials can be employed as the base in these devices. In the ANE case, the Ettingshausen heat current is generated by the electric current from the low-temperature side to the high-temperature side. This current increases the conversion rate efficiency, because Ettingshausen heat current and the electric current directions are perpendicular to each other [2] as shown in Fig. 1.1 (b).

1.2 An Overview of Anomalous Nernst Effect

The electric field of ANE in the nanostructured magnetic materials is induced by the interplay of magnetization and temperature gradient. This condition explains that the thermoelectric voltage in magnetic materials is observable although there are small temperature gradients at room temperature. The thermoelectric voltage is strongly dependent on the crystallographic orientation [3], material type, layer thickness in the geometry film [4], and magnetic anisotropy [5]. However, even though there are many recent advances in ANE research, there are several aspects of the correlation between ANE and nanostructured ferromagnetic materials that

have not fully explored yet such as the origin of large anomalous Nernst coefficient in the ferromagnetic materials.

The large ANE magnitude usually is occurred in the magnetic materials which have a large thermoelectric coefficient. The thermoelectric coefficient depends on the product of the Seebeck coefficient and Hall ratio. It is also related to the anomalous Hall conductivity (AHC) asymmetry as a function of chemical potential [6, 7]. The AHC mechanism is determined by intrinsic and extrinsic contributions. Band structure dictates the intrinsic contribution of AHC because the electron anomalous velocity related to the Berry curvature is increased by interband coherence [8]. Moreover, one of the extrinsic contributions of AHE is the skew scattering which is generated from the impurity or the effective spin-orbit interaction [9]. This extrinsic contribution is reported experimentally in ANE magnitude of $\text{La}_{1-x}\text{Na}_x\text{MnO}_3$ [10]. However, the anomalous Nernst coefficient (ANC) sometimes is not determined by AHC. AHC is influenced by Berry curvature summation of all occupied states while ANE is determined by Berry curvature at low temperature [13, 12, 11]. In other words, observing the material which possesses large Berry curvature is important to step for achieving large ANC.

1.3 Anomalous Nernst Effect Based in the 2D Magnetic Materials

The realization of thermoelectric devices challenge is to ensure the materials exhibiting high ANC values. Using 2D materials is one of the solution for this problem. For example, the EuO monolayer is shown that it possesses a large ANC [7, 14]. In 2D materials, the ANE is associated to the quantum anomalous Hall effect. AHC in the 2D system is influenced by the quantized anomalous Hall conductivity (AHC), which can be denoted by $\sigma_{xy} = \frac{e^2}{h}C$, where C is Chern number. The quantized AHC was proved experimentally by Chang et al. [15] in a magnetically doped thin film of a topological insulator $(\text{Bi}, \text{Sb})_2\text{Te}_3$. Their results suggest that it is possible to found a large ANC in 2D systems.

A high figure of merit can be accomplished by 2D ANE thermoelectric materials which several reasons. The study of the ANE in 2D systems is opened by the discovery of ferromagnetism (FM) in 2D materials in 2017 [16, 17]. The use of a 2D material has a role in decreasing the thermal conductivity due to surface phonon scattering [18] which is essential for increasing the figure of merit. The use of some 2D material also provides that the electrical conductivity is higher than that of the corresponding bulk structure while the material thickness decreasing. [19]. Besides that, the thermoelectric coefficient for quantum-well structures enhanced

linearly when the quantum-well thickness reduced [20]. These advantage of 2D thermoelectric devices has been proved experimentally by Lee et al. using 2D SnS_2 [21] and Ohta et al. using 2D gas in SrTiO_3 [22].

In this study, we explored the thermoelectric properties of a half-metallic 1T- FeCl_2 monolayer by using density functional calculations. We obtain that the 1T- FeCl_2 monolayer possesses high AHC, which generates a large ANC. The high AHC has resulted from the bands at the K-point near the Fermi level, where a large Berry curvature exists. In addition, the thermoelectric properties of the 1T- FeCl_2 monolayer can be tuned by charge doping. By this approach, we obtain a large ANC at the Fermi level. Based on this, it can be concluded that 2D magnetic half-metallic materials generate high ANC values.

1.4 The Purpose of This Study

We have some purposes in this study. First, we explore the magnetic and electronic properties of 1T- FeCl_2 monolayer. The results of magnetic and electronic properties lead to analyze the thermoelectric properties of 1T- FeCl_2 monolayer. From that, we examine how to tune the thermoelectricity in this material. Subsequently, we also explore the origin of ANC in the of 1T- FeCl_2 monolayer.

1.5 Outline of Dissertation

This dissertation consists of five chapters. In chapter 1, the motivation which is related to the anomalous Nernst effect in the 2D magnetic materials is presented. An overview of anomalous Nernst effect is given including its origin magnitude. After that, the 2D ferromagnetic material related to the anomalous Nernst effect is explored and also the purpose of this study is explained in this chapter.

In chapter 2, the basic concepts of the origin magnetism and anomalous Nernst effect in the 2D magnetic materials are described. The fundamental concepts of density functional theory and the algorithm of maximally localized Wannier function are also presented. Furthermore, We provide the computational scheme, which is related to the practical calculation in this study.

In chapter 3, we show the calculated results of the atomic structure of 1T- FeCl_2 monolayer. This atomic structure will then affect the magnetic properties of a 1T- FeCl_2 monolayer based on the Goodenough-Kanamori-Anderson rules. Moreover, we show that the half-metallic is occurred in the 1T- FeCl_2 monolayer and we also explain its origin.

In chapter 4, we explored the thermoelectric properties of a 1T- FeCl_2 monolayer. We show that 1T- FeCl_2 monolayer possesses a large anomalous Nernst coefficient. Its

magnitude is originated from anomalous Hall conductivity. The origin of anomalous Hall conductivity is then described by including the band contribution near the Fermi level.

Finally, in chapter 5, we give a summary of this study. we also explain the future scope such as the effect of the vacuum region and the calculation in the large supercell with the charge doping. We plan to include the relaxation time calculation which essential in determining the anomalous Nernst coefficient.

Chapter 2

Background: Basic Theory and Computational Methods

2.1 Density Functional Theory (DFT)

In condensed matter physics, the various properties of the materials can be explored by analyzing the electron interactions. In the material which consists of many-electron and nuclei, the many-body problems are related with time-independent Schödinger equation with $3M+3N$ parameter space dimension which expressed as

$$H\Psi(r_1, r_2, \dots, R_1, R_2, \dots) = E\Psi(r_1, r_2, \dots, R_1, R_2, \dots), \quad (2.1)$$

where Ψ is the system wave function, r_i and R_i are the electron and nucleus positions respectively, and H is the Hamiltonian of the system which can be written as

$$H = -\sum_i \frac{\nabla_i^2}{2} - \sum_{i,I} \frac{Z_I}{|r_i - R_I|} + \frac{1}{2} \sum_{i \neq j} \frac{1}{|r_i - r_j|} - \sum_I \frac{\nabla_i^2}{2M_I} + \frac{1}{2} \sum_{I \neq J} \frac{Z_I Z_J}{|R_I - R_J|}, \quad (2.2)$$

where the Z_I and M_I are charge and mass of the nucleus, respectively. For simplicity, $\hbar = m_e = e = 4\pi\epsilon_0 = 1$ and the Eq. (2.2) can be divided by five terms which are denoted by

$$H = T_{el} + V_{el-nuc} + V_{el-el} + T_{nuc} + V_{nuc-nuc}, \quad (2.3)$$

where T_{el} and T_{nuc} are the kinetic energy operator of electron and nucleus, respectively. V_{el-nuc} represents the potential energy operator between electron and nucleus, V_{el-el} and $V_{nuc-nuc}$ are the Coulomb interaction operator of electron-electron and nucleus-nucleus, respectively.

Because of the defined dimension in Eq. (2.1) is complex to be solved except for the simplest system such as hydrogen atom, the approximation has to be applied. Since the mass of the nucleus is heavier than electrons, the nucleus motion can be neglected compared to those of electrons. In other words, the nucleus is defined that its position is fixed and its movement is stationary. This approximation is known as the Born-Oppenheimer approximation. In this case, T_{nuc} and $V_{nuc-nuc}$ in Eq. (2.3) are ignored so that the Eq. (2.3) becomes

$$H = T_{el} + V_{el-nuc} + V_{el-el}, \quad (2.4)$$

According to this modification, the new Schödinger equation of the system can be expressed as

$$H\Psi = \left[-\sum_i \frac{\nabla_i^2}{2} - \sum_{i,I} \frac{Z_I}{|r_i - R_I|} + \frac{1}{2} \sum_{i \neq j} \frac{1}{|r_i - r_j|} \right] \Psi = E\Psi. \quad (2.5)$$

In this equation, $\Psi = \Psi(r_1, r_2, \dots)$ is wave function of many electrons.

One of the method which can solve many-electron system is Hartree approximation. This approximation defines Eq. (2.4) as a one-particle equation for an electron moving in an average potential of all the electrons. In this condition, the wave function can be donated as multiplication of n independent electron wave function $\psi(r_n)$ which expressed by

$$\Psi(r_1, r_2, \dots, r_n) = \psi(r_1)\psi(r_2)\dots\psi(r_n). \quad (2.6)$$

By inserting the Eq.(2.6) into Eq.(2.5), the Hartree equation can be obtained which described by

$$\left[-\sum_i \frac{\nabla_i^2}{2} - \sum_{i,I} \frac{Z_I}{|r_i - R_I|} + \sum_{i \neq j} \int d^3r_j \frac{|\psi_j(r_j)|^2}{|r_i - r_j|} \right] \psi_i = \epsilon_i \psi_i(r_i) \quad (2.7)$$

In Eq. (2.7), each electron i is treated independently but in an effective potential, which is determined by an integration over the wave function of the other electron. Since for the i^{th} wave function, the effective potential depends on all the other wave functions, we can solve Eq. (2.7) by using the self-consistent method. In this method, the wave function for the step k can be found by solving the Eq. (2.7) with the effective potential is determined by the wave function in the step of $k - 1$. Beside of that, By applying the variational principle, the condition of $\frac{\langle \psi | H | \psi \rangle}{\langle \psi | \psi \rangle} \geq E_0$ is satisfied for any wave function ψ where E_0 is the ground states energy of the system. This procedure is repeated until all the wave functions converge to a solution.

There is one problem in the Hartree approximation. This approximation does not satisfy the Pauli exclusion principle because only symmetric wave functions used

in the calculation. It means that this method does not include exchange interaction. Because of that, Hartree and Fock formulate the approximation which can explain electron as a distinguishable particle in the calculation. By using Slater determinant, the n-electron system wave function is treated by an anti-symmetric wave function which can be seen as

$$\Psi(r_1, r_2, \dots, r_n) = \frac{1}{\sqrt{n!}} \begin{bmatrix} \psi_1(r_1) & \psi_1(r_2) & \dots & \psi_1(r_n) \\ \psi_2(r_1) & \psi_2(r_2) & \dots & \psi_2(r_n) \\ \vdots & \vdots & \ddots & \vdots \\ \psi_n(r_1) & \psi_n(r_2) & \dots & \psi_n(r_n) \end{bmatrix}. \quad (2.8)$$

By applying the variational principle with the Eq. (2.8), the Eq.(2.7) is updated which can be written as

$$\left[-\sum_i \frac{\nabla_i}{2} - \sum_{i,I} \frac{Z_I}{|r_i - R_I|} + \sum_{i \neq j} \int d^3 r_j \frac{|\psi_j(r_j)|^2}{|r_i - r_j|} \right] \psi_i - \left[\sum_j \int d^3 r_j \psi_j^*(r_j) \frac{1}{|r_i - r_j|} \psi_i(r_j) \right] \psi_j = \epsilon_i \psi_i(r_i). \quad (2.9)$$

In the Eq. (2.9), there is a new term that is denoted as exchange potential. However, in this equation, the correlation energy due to many-body interaction is ignored, which produces an incorrect description of the electronic properties. Because of that, it is required methods that can deal with both exchange interaction and correlation energy.

As mentioned before that the electronic structure of the many-body system can be described by incorporating the effect of both exchange and correlation. Therefore, an efficient computational scheme is necessary. Recently, the density functional theory (DFT) is one of the most popular approaches for explaining the exchange and correlation problem. DFT is a computational method that determined the properties of many-electron systems by using functionals of ground-state electron density. DFT method also is applied for calculating, e.g., the binding energy of molecules in chemistry and the electronic band structure of solids in physics. The development of DFT is based on Hohenberg-Kohn theorem[23]:

Theorem 1. *For any system of interacting particles in external potential $V_{ext}(\mathbf{r})$ apart from a trivial additive constant, the potential $V_{ext}(\mathbf{r})$ is uniquely determined by the ground state of electron density $n_0(\mathbf{r})$.*

This first theorem explains that all of the electronic properties can be picked up from the exact ground-state electron density. Then, the ground-state electron

density can be obtained by applying the second theorem, which is based on the variational principle which is described by

Theorem 2. *For any $V_{ext}(\mathbf{r})$, a universal functional exist for the total energy functional $E[n]$ that its global minimum value gives the exact ground state energy of the system, while the minimizing density $n(\mathbf{r})$ is the exact ground state density $n_0(\mathbf{r})$.*

In the second theorem, all the ground state properties can be obtained by minimizing energy functional with respect to electron density. This energy functional is expressed as

$$E_{HK}[n] = T[n] + \int V_{ext}(\mathbf{r})n(\mathbf{r})d^3r + E_{II} + E_{int}[n], \quad (2.10)$$

with $T[n]$, E_{II} , and $E_{int}[n]$ correspond to kinetic energy, interaction energy of nuclei, and potential energy of the interacting system respectively. It should be noted that this formulation is applied in $T = 0$ K. Also, the problem still remains as the exact functionality is unknown. The Kohn-Sham approach is used to overcome this problem by replacing the interacting-electrons system with a non-interacting independent-electron system that is under the influence of an effective potential. The Kohn-Sham energy functional can be written as[24]

$$E_{KS}[n] = T_s[n] + \int V_{ext}(\mathbf{r})n(\mathbf{r})d^3r + E_{II} + E_H[n] + E_{XC}[n], \quad (2.11)$$

with the kinetic energy of non-interacting electrons $T_s[n]$ is denoted by

$$T_s[n] = \sum_i \int \Psi_i^*(\mathbf{r}) \left(-\frac{1}{2} \nabla^2 \right) \Psi_i(\mathbf{r}) d\mathbf{r}, \quad (2.12)$$

and the Hartree energy E_H which contain the electrostatic interaction is expressed as

$$E_H[n] = \frac{1}{2} \int \frac{n(\mathbf{r})n(\mathbf{r}')}{|\mathbf{r} - \mathbf{r}'|} d\mathbf{r}d\mathbf{r}'. \quad (2.13)$$

Based on this approach, now the exchange and correlation interactions are grouped into the exchange-correlation energy E_{XC} . E_{XC} has an important role here. When E_{XC} is evaluated, the ground state density and the energy of the many-body system can be obtained.

Considering the fact that the Kohn-Sham energy problem is a minimization problem with respect to the density $n(r)$, the solution can be obtained by performing a functional derivative. By applying a variational theorem of the energy functional E_{KS} with respect to the wavefunctions, Kohn-Sham equation based on the many-

body Schrödinger equation can be obtained as

$$\left(-\frac{1}{2}\nabla^2 + V_{eff}(\mathbf{r})\right)\Psi_i(\mathbf{r}) = \epsilon_i\Psi_i(\mathbf{r}). \quad (2.14)$$

The Kohn-Sham equation is defined by a local effective potential V_{eff} in which the non-interacting particles move. The effective potential then can be expressed as[24]

$$V_{eff}(\mathbf{r}) = V_{ext}(\mathbf{r}) + V_H(\mathbf{r}) + V_{XC}(\mathbf{r}), \quad (2.15)$$

with

$$V_H(\mathbf{r}) = \frac{1}{2} \int \frac{n(\mathbf{r}')}{|\mathbf{r} - \mathbf{r}'|} d\mathbf{r}'. \quad (2.16)$$

$V_{ext}(r)$ and $V_H(r)$ depends on $n(r)$. It indicates that $V_{ext}(r)$ and $V_H(r)$ will also depend Ψ_i . Because of that, the solution of the Kohn-Sham equation can be found by self-consistent methods. The self-consistent of Kohn-Sham equation is schematically shown in Fig. (2.1). It is started from an initial guess of $n(r)$, then calculating the corresponding $V_{ext}(r)$ and $V_H(r)$ and obtaining V_{eff} . Subsequently, the solution of Ψ_i can be evaluated by solving the Kohn-Sham equation. Moreover, a new density, which is obtained by the results of Ψ_i is applied as an initial new guess for $n(r)$, and it also used to calculate the new V_{eff} . This schematic is repeated until the convergence is satisfied.

There is still problem in the DFT calculation which is how to find the exchange-correlation energy E_{XC} . This functional term is not known except for the free electron gas. Therefore, it is required for obtaining accurately E_{XC} in order to satisfy the realistic condensed-matter system description. For the homogeneous electron system, the functional of $E_{XC}[n]$ depends only on the density. However, in the non-homogeneous electron system, $E_{XC}[n]$ at point r is not only depends on the density at r , but it also depends on the variation at near r . There are many approximations to find an accurate $E_{XC}[n]$. The well-known approximations are including the local density approximation (LDA) and the generalized gradient approximation (GGA).

The simplest method to approximate $E_{XC}[n]$ is the local density approximation (LDA). In this approximation, there is two important points which are assumed: i) the local exchange-correlation energy per particle only depends on the local density, and ii) it is equal to the exchange-correlation energy per particle of a homogeneous electron gas, which has the same density in the neutralizing positive background. $E_{XC}[n]$ is then given by the sum of the contributions of each point in space, where it is assumed that the contribution of one point only depends on the density of that particular point and it is independent of the other points. The exchange-correlation for LDA functional V_{XC}^{LDA} is expressed as

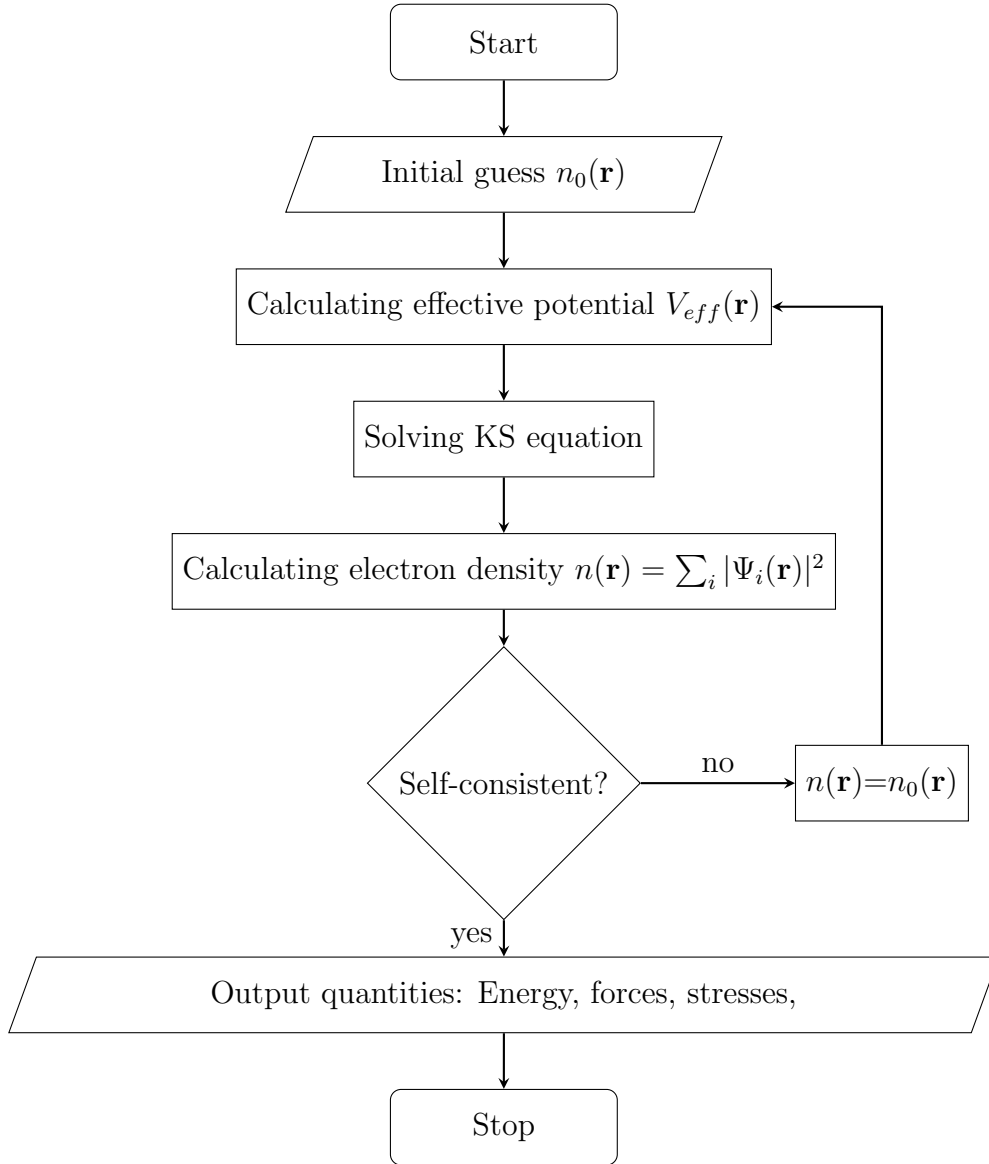


Figure 2.1: The schematics of Kohn-Sham equation self-consistent calculation.

$$V_{XC}^{LDA} = \epsilon_{XC}(n(\mathbf{r})) + n(\mathbf{r}) \frac{\partial \epsilon_{XC}(n(\mathbf{r}))}{\partial n(\mathbf{r})}, \quad (2.17)$$

The LDA approximation is assumed that the density is locally constant so that it is more accurate for the system which has slowly varying densities. In binding energy which reflected across the periodic table, LDA always generates precise results. Besides that, several physical properties such as vibrational energies, bond length, atomic structures are predicted correctly although with some reasonable deviation. However, several binding energies of solids and molecules are sometimes overestimated, which leads to an underestimation of the bond lengths. LDA also sometimes is underestimated the bandgap.

In the real system, the density varies in the space. The functional change rate should be included. It can be obtained by adding gradient terms. This ap-

proach is called as the gradient expansion approximation. In this approximation, the gradient corrections of the form $\nabla_n(r)$, $|\nabla_n(r)|^2$, and $|\nabla_n^2(r)|$ is combined to the LDA exchange-correlation energy functionals. The general form of the exchange-correlation energy functionals in GGA is written as

$$V_{XC}^{GGA} = \epsilon_{XC}(n(\mathbf{r})) + n(\mathbf{r}) \frac{\partial \epsilon_{XC}(n(\mathbf{r}))}{\partial n(\mathbf{r})} - \nabla \left(n(\mathbf{r}) \frac{\partial \epsilon_{XC}(n(\mathbf{r}))}{\partial \nabla n(\mathbf{r})} \right). \quad (2.18)$$

2.2 Norm Conserving Pseudo-potential and Pseudo-atomic Basis Orbitals

Replacing the effect of the core electrons with an effective potential is a key concept of pseudo-potential. Solving the atomic problem with Khon-Sham (KS) approach is the first procedure of the pseudo-potential generation. The distinction between valence and core states can be obtained when the KS orbitals are found from the solution of the KS equation. we can assume that the core states are altered very small due to the environment changes. These effects can be replaced by using a model potential derived from the atomic configuration. Besides that, the valence states are shown to oscillate rapidly to the core regions. Moreover, the valences states are expected to be smoother by introducing the new potential.

Assuming that the core states and the core eigenvalues of Hamiltonian H are defined by $|\chi_n\rangle$ and E_n , respectively. It is also defined that the valence states can be replaced by the smoother wave function $|\phi\rangle$ and expands the remaining portion in terms of core states,

$$|\Psi\rangle = |\phi\rangle + \sum_n^{core} a_n |\chi_n\rangle. \quad (2.19)$$

By calculating the inner product of Eq. (2.19) with $|\chi_n\rangle$ and by defining the valence states $|\Psi\rangle$ is orthogonal to the $|\chi_n\rangle$, the Eq. (2.19) relation is written as

$$\langle \chi_n | \Psi \rangle = \langle \chi_n | \phi \rangle + \sum_n^{core} a_n \langle \chi_m | \chi_n \rangle = 0. \quad (2.20)$$

Now we can write the right-hand side of Eq. (2.20) in term of smoother function,

$$|\Psi\rangle = |\phi\rangle - \sum_n \langle \chi_m | \phi | \chi_n \rangle. \quad (2.21)$$

By applying \mathbf{H} into Eq. (2.21), we will get

$$H|\Psi\rangle + \sum_n (E - E_n)|\chi_n\rangle \langle\chi_n|\phi\rangle = E|\phi\rangle. \quad (2.22)$$

Eq. (2.22) indicates that smoother function satisfies an effective equation with the same eigen energy of the real valence wave function. From that, the new eigenvalues for the smoother function $|\phi\rangle$ can be written as

$$(H + V_{n,l})|\phi\rangle = E|\phi\rangle. \quad (2.23)$$

Because of the spherical symmetry, $V_{n,l}$ depends on the angular momentum quantum number l and its effect is localized to the core.

There are some requirements for norm-pseudopotential which will be used. First, all the electrons (AE) and pseudo (PS) valence eigenvalues are equal to the selected atomic configuration. Second, all the electrons (AE) and pseudo (PS) valence eigenfunctions are in agreement in the external core region which described by

$$\Psi_i^{AE}(r) = \Psi_i^{PS}(r), r \geq r_{core}. \quad (2.24)$$

The logarithmic derivatives and their first energy derivative of real and pseudo wave functions are also in agreement which denoted by

$$\left[\frac{d}{dr} \ln \Psi_i^{AE}(r) \right]_R = \left[\frac{d}{dr} \ln \Psi_i^{PS}(r) \right]_R, R \leq r_{core}. \quad (2.25)$$

Furthermore, the total charge inside of the core radius ($R \leq r_{core}$) for each wave function must be same which is due to norm conservation.

$$\int_0^R |\Psi_i^{AE}(r)|^2 dr = \int_0^R |\Psi_i^{PS}(r)|^2 dr. \quad (2.26)$$

In the OpenMX code [25], KS wave functions Ψ_n are expanded by the linear pseudo-atomic orbitals (LPAO) $\phi_{i,\alpha}$ [26] which can be written as

$$\Psi_\mu(r) = \sum_i^\alpha c_{\mu,i,\alpha} \phi_{i,\alpha}(r - r_i), \quad (2.27)$$

where α is the orbital index and i is the site index. Here $\phi_{i,\alpha}$ is consist of radial wave function $R_{i,p,l}(r)$ and spherical harmonic wave function $Y_{l,m}(\theta, \phi)$ which is written as

$$\phi_{i,\alpha} \equiv R_{i,p,l}(r) Y_{l,m}(\theta, \phi). \quad (2.28)$$

$R_{i,p,l}(r)$ depends on the angular quantum number l , the site index i , and the multi-

plicity index p while $Y_{l,m}(\theta, \phi)$ depends on the magnetic quantum number m and l . $R_{i,p,l}(r)$ is also defined as a primitive orbitals.

$R_{i,p,l}(r)$ can be generated by some conditions. The atomic orbitals must completely vanish within a cutoff radius. It should be continued up to the third derivatives around the cutoff radius so that matrix elements for the kinetic operator are also continuous up to the first derivatives. A few parameters can be applied to generate as many as possible a set of atomic orbitals. The atomic core potential $V_{core}(r)$ in the all-electron calculation can be modified in the generation of pseudopotential, which is denoted by

$$V_{core}(r) = \begin{cases} -\frac{Z}{r} & r \leq r_1 \\ \sum_0^3 b_n r^n & r_1 < r \leq r_c \\ h & r_c < r \end{cases} \quad (2.29)$$

where b_0 , b_1 , b_2 , and b_3 are constants, which is determined in the condition that the value and the first derivative are continuous at both r_1 and r_c .

2.3 Non-collinear Density Functional Theory

The non-collinear DFT methods is applied to investigate the effect of spin-orbit interaction (SOI). In the non-collinear DFT, two components spinor wave functions are expressed by

$$\Psi_\nu = |\Psi_\nu^\alpha\rangle|\alpha\rangle + |\Psi_\nu^\beta\rangle|\beta\rangle, \quad (2.30)$$

where $|\Psi_\nu^\alpha\rangle$ is a spatial function and $|\alpha\rangle$ is a spin function. From this, it can be defined as the density operator which can be expressed as

$$\hat{n} = \sum_\nu f_\nu |\Psi_\nu\rangle\langle\Psi_\nu| = \sum_\nu f_\nu (|\Psi_\nu^\alpha\rangle|\alpha\rangle + |\Psi_\nu^\beta\rangle|\beta\rangle)(\langle\Psi_\nu^\alpha| \langle\alpha| + \langle\Psi_\nu^\beta| \langle\beta|), \quad (2.31)$$

where f_ν is a step function which is defined as the Fermi distribution function on the OpenMX code. From the Eq. (2.31), the non-collinear density electron in the real space is denoted by

$$n_{\sigma\sigma'} = \langle r\sigma | \hat{n} | r\sigma' \rangle = \sum_\nu f_\nu \Psi_\nu^\sigma \Psi_\nu^{\sigma'*}, \quad (2.32)$$

where σ and σ' ($= (\alpha, \beta)$) are eigenfunction of position vector. Next, the up and down densities at each point are calculated by diagonalizing non-collinear density matrices which can be written as

$$\begin{pmatrix} n'_\uparrow & 0 \\ 0 & n'_\downarrow \end{pmatrix} = U n U^\dagger = U \begin{pmatrix} n_{\alpha\alpha} & n_{\alpha\beta} \\ n_{\beta\alpha} & n_{\beta\beta} \end{pmatrix} U^\dagger, \quad (2.33)$$

where n'_\uparrow and n'_\downarrow indicate the up-densities and down-densities, respectively. Here, the U -matrix in Eq. (2.33) is introduced as a rotation operator D which is given by

$$D \equiv \exp(-i\hat{\sigma}_i \cdot \hat{h}\phi/2) \quad (2.34)$$

where \hat{h} is a unit vector along a certain direction, ϕ is the rotational angle around \hat{h} , and $\hat{\sigma}_i$ is Pauli matrices which expressed as

$$\sigma_1 = \begin{pmatrix} 0 & 1 \\ 1 & 0 \end{pmatrix}, \sigma_2 = \begin{pmatrix} 0 & -i \\ i & 0 \end{pmatrix}, \sigma_3 = \begin{pmatrix} 1 & 0 \\ 0 & -1 \end{pmatrix}. \quad (2.35)$$

If the rotation is defined along the z-axis with Euler angle (θ, ϕ) , D becomes

$$D(\theta, \phi) = \begin{pmatrix} \exp(-i\frac{\phi}{2})\cos(\frac{\theta}{2}) & -\exp(-i\frac{\phi}{2})\sin(\frac{\theta}{2}) \\ \exp(i\frac{\phi}{2})\sin(\frac{\theta}{2}) & \exp(i\frac{\phi}{2})\cos(\frac{\theta}{2}) \end{pmatrix}. \quad (2.36)$$

According to Eq. (2.36), the U matrix can be obtained by the conjugate transposed matrix of D which is denoted by

$$D(\theta, \phi) = \begin{pmatrix} \exp(i\frac{\phi}{2})\cos(\frac{\theta}{2}) & \exp(-i\frac{\phi}{2})\sin(\frac{\theta}{2}) \\ -\exp(i\frac{\phi}{2})\sin(\frac{\theta}{2}) & \exp(-i\frac{\phi}{2})\cos(\frac{\theta}{2}) \end{pmatrix}. \quad (2.37)$$

The total energy non-collinear functional can be obtained by using Eq.(2.30), Eq.(2.32), and Eq.(2.33) which given by

$$E_{total} = \sum_{\sigma=\alpha,\beta} \sum_{\nu} f_{\nu} \langle \Psi_{\nu}^{\sigma} | \hat{T} | \Psi_{\nu}^{\sigma} \rangle + \sum_{\sigma\sigma'} \int w_{\sigma\sigma'} n_{\sigma\sigma'} + \frac{1}{2} \int \int \frac{n'(r)n'(r')}{|r-r'|} d\nu d\nu' + E_{xc}. \quad (2.38)$$

The first and second term in the Eq. (2.38) indicate the kinetic energy and Coulomb interaction energy between electron and core, respectively. Besides that, the third and fourth terms in Eq. (2.38) represent Coulomb interaction energy between electron-electron and the exchange-correlation energy, respectively. The Eq. (2.38) also can be simplified which given by

$$E_{total} = E_{band} - \frac{1}{2} \int n' V_H d\nu - \int Tr(V_{xc} n) + E_{xc} \quad (2.39)$$

where V_{xc} is a non-collinear exchange-correlation potential and $V_H = \int \frac{dr}{|r-r'|} d\nu$.

Now, we introduce a new functional F which relates to the orthogonality of the

spinor wave functions expressed by

$$F = E_{total} + \sum_{\sigma\sigma'} \epsilon_{\sigma\sigma'} (\delta_{\sigma\sigma'} - \langle \Psi_\nu | \Psi'_\nu \rangle). \quad (2.40)$$

The variational of F is related with the spatial wave function Ψ_ν^σ which is given by

$$\frac{\delta F}{\delta \Psi_u^{\sigma,*}} = \hat{T} \Psi_u^\sigma + \sum_{\sigma'} w_{\sigma\sigma'} \Psi_u^{\sigma'} + V_H \Psi_u^\sigma + \sum_{\sigma'} V_{xc}^{\sigma\sigma'} \Psi_u^{\sigma'} - \sum_\nu \epsilon_{u\nu} \Psi_\nu^\sigma. \quad (2.41)$$

with

$$V_{xc}^{\sigma\sigma'} = \frac{\delta E_{xc}}{\delta n_{\sigma\sigma'}}. \quad (2.42)$$

Here the functional of F will be minimum, if its variation with respect to the Ψ_ν^σ vanishes. By using a unitary transformation of Ψ_ν^σ to diagonalize $\epsilon_{u\nu}$, the non-collinear KS equation can be found as follows

$$\begin{pmatrix} \hat{T} + w_{\alpha\alpha} + V_H + V_{xc}^{\alpha\alpha} & w_{\alpha\beta} + V_{xc}^{\alpha\beta} \\ w_{\beta\alpha} + V_{xc}^{\beta\alpha} & \hat{T} + w_{\beta\beta} + V_H + V_{xc}^{\beta\beta} \end{pmatrix} \begin{pmatrix} \Psi_u^\alpha \\ \Psi_u^\beta \end{pmatrix} = \epsilon_u \begin{pmatrix} \Psi_u^\alpha \\ \Psi_u^\beta \end{pmatrix}. \quad (2.43)$$

In the Eq.(2.43), It is shown that there is the interaction between α and β spin components which coupled each other in the off-diagonal part. In this part, there are V_{xc} and the other new contribution w .

2.4 Maximally Localized Wannier Functions

Generally, the electronic ground states can be expressed in terms of Bloch orbitals by labeled their position in reciprocal space and their energy band. These Bloch orbitals are localized in energy in the line that there are eigenstates to the Hamiltonian. The Bloch orbitals have an indeterminacy regarding both the overall phase and the choice of gauge, meaning that any arbitrary unitary transformation of the Bloch orbitals will yield the same physics. Therefore, the Wannier functions can be expressed as a superposition of Bloch orbitals which calculated through a series of unitary transformations [27].

Wannier functions were found to be useful for a starting point in semi-classical electron dynamics calculation. These functions also can be applied for evaluating tight-binding Hamiltonians as well as providing the chemical bonding of the crystals. These Wannier functions are strongly non-unique due to the indeterminacy of the Bloch orbitals and the natural choice is to choose the Wannier functions that are maximally localized. In order to find the maximally localized Wannier function, the

Wannier function in which the localization functional reaches its global minimum is required.

There are several steps in the maximally Wannier functions calculation algorithm. First, the Bloch orbitals can be expressed as

$$|\Psi_{nk}\rangle = |u_{nk}\rangle \exp(ik \cdot r), \quad (2.44)$$

where $|u_{nk}\rangle$ has the same periodicity as the electrical potential, r is the location in real space, k is the wave vector in the Brillouin zone, n is the band number. From this, the smooth trial function $|g_n\rangle$ is defined. Then, the new Bloch orbital can be denoted by

$$|\phi_{nk}\rangle = \sum_{m=1}^J |\Psi_{mk}\rangle \langle \Psi_{mk} | g_n \rangle. \quad (2.45)$$

The Eq.(2.45) can be normalized into smooth orthonormal Bloch orbital which is written as

$$|\tilde{\phi}_{nk}\rangle = \sum_{m=1}^J |\Psi_{mk}\rangle * \langle \Psi_{mk} | \Psi_{nk} \rangle_V^{-\frac{1}{2}}. \quad (2.46)$$

From this, the new $|u_{nk}\rangle$ is extracted which given by

$$|u_{nk}\rangle = |\tilde{\Psi}_{nk}\rangle \exp(-ik \cdot r). \quad (2.47)$$

Therefore, the overlap matrix can be described by

$$M_{mn}^{k,b} = \langle u_{nk} | u_{nk+b} \rangle. \quad (2.48)$$

The operators $R_{mn}^{k,b}$ and $T_{mn}^{k,b}$ are defined by

$$R_{mn}^{k,b} = M_{mn}^{k,b} M_{nn}^{k,b*} \quad (2.49)$$

$$T_{mn}^{k,b} = \frac{M_{mn}^{k,b}}{M_{nn}^{k,b}} * (Im(\ln(M_{mn}^{k,b})) - b \cdot (\sum_b w_b b * Im(\ln(M_{nn}^{k,b}))). \quad (2.50)$$

The crystal structure is then divided into shells at each point in k -space and the vector b_α is defined as the vector going between the central k -point and a neighbor in shell α . A number of shells are then chosen so that the condition

$$\sum_b w_b b_\alpha b_\beta = \delta_{\alpha\beta} \quad (2.51)$$

can be satisfied for some weight w_b . If the crystal is a cubic lattice, then only one shell requires to be used and $w_b = 3/Zb^2$ where Z is the number of neighbors in the

shell. A starting point for the unitary transformation steps is then defined by

$$U_{mn}^k = \delta_{mn}. \quad (2.52)$$

A step for the unitary transformation is then calculated which denoted by

$$\Delta W = \frac{\alpha}{\sum_b w_b} \sum_b w_b (A(R^{(k,b)}) - S(T^{(k,b)})), \quad (2.53)$$

for some constant α . Here, A and S are defined as super operators. The unitary transformation is then updated using this step.

$$U_{mn}^k \rightarrow U_{mn}^k e^{\Delta W}. \quad (2.54)$$

After this step, the overlap matrix is updated by using the unitary transformation which expressed as

$$M_{mn}^{(k,b)} \rightarrow U_{mn}^{(k)\dagger} M_{mn}^{(k,b)} U_{mn}^{(k)}. \quad (2.55)$$

A new step can now be calculated using the new overlap. This is iterated until convergence has been obtained. The overlap does then correspond to the maximally localized Wannier function and the Wannier function can be calculated using

$$|0n\rangle = \frac{V}{2\pi} \int_{BZ} |u_{nk}\rangle e^{ik \cdot r} dk \quad (2.56)$$

2.5 Octahedral Crystal Field Theory and Super Exchange Interaction

The breaking of orbital degeneracy in transition metal complexes due to the presence of ligands can be explained by crystal field theory. Ligands are ions or neutral molecules that bond to a central metal atom or ion. Ligands have at least one donor atom with an electron pair used to form covalent bonds with the central atom. The strength of the metal-ligand bonds can be evaluated qualitatively by crystal field theory. Based on the strength of the metal-ligand bonds, the energy of the system can be adjusted. This may also lead to a change in magnetic properties as well as color. This theory was developed by Hans Bethe and John Hasbrouc van Vleck [28].

As a simplification, it is assumed that the ions are simple point charges. The approach taken uses classical potential energy equations that take into account the attractive and repulsive interactions between charged particles which are known as Coulomb's Law interactions. For transition metal cations, the shape and occupation of its d -orbitals become important for explaining the bond energy and both magnetic and electronic properties of the transition metal compound.

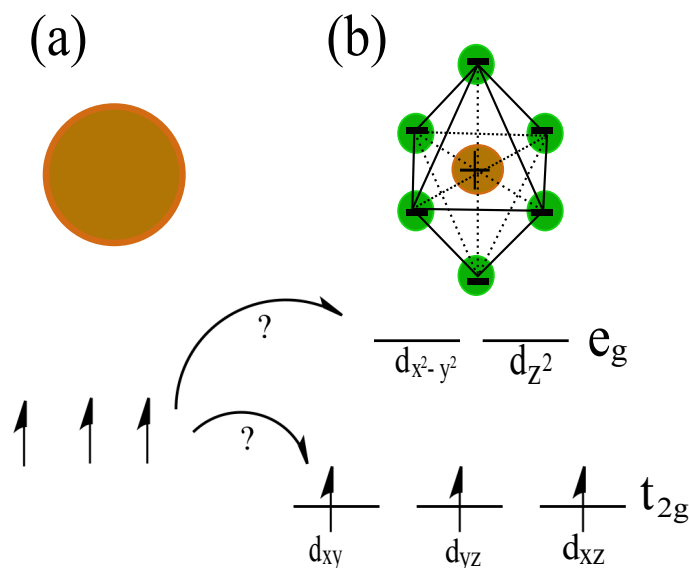


Figure 2.2: The different of (a) single transition metal orbital energy and (b) when ligands approach the transition metal ion which forming octahedral structure

As we know that a single transition metal ion has the same energy in the five d -orbitals as shown in Fig. 2.2 (a). However, when ligands hybridize the metal ion, it will be affected the condition of the d -orbital electron and it will be based on the geometric structure of the molecule. Since ligands approach from different directions, not all d -orbitals interact directly. This condition will be caused the splitting energy between d -orbitals due to Coulomb interaction.

For example, consider a molecule with octahedral geometry as shown in Fig. 2.2(b). Ligands bond the metal ion along the x , y , and z axes. Therefore, the electrons in the d_{z^2} and $d_{x^2-y^2}$ orbitals experience greater repulsion due to directly interacting with ligands orbitals. It also requires more energy to have an electron in these orbitals than it would put an electron in one of the other orbitals. This causes a splitting in the energy levels of the d -orbitals. This is known as crystal field splitting. For octahedral complexes, crystal field splitting is denoted by J . The energies of the d_{z^2} and $d_{x^2-y^2}$ orbitals increase due to greater interactions with the ligands. Beside of that, because d_{xy} , d_{xz} , and d_{yz} orbitals are indirectly connected with the ligands orbital, their energies are more stable.

According to the Aufbau principle, electrons are filled from lower to higher energy orbitals. Following Hund's rule, electrons are filled in order to have the highest number of unpaired electrons. For example, if one had a d^3 , there will be three unpaired electrons. If the electron is added, there is some explanation of how to fill a higher energy orbital (d_{z^2} or $d_{x^2-y^2}$) or pair with an electron in the d_{xy} , d_{xz} , or d_{yz} orbitals. This pairing of the electrons requires energy. If the pairing energy is less than the crystal field splitting energy, J , then the next electron will occupy into the d_{xy} , d_{xz} , or d_{yz} orbitals due to stability. This condition allows for the least

amount of unpaired electrons and is known as a low spin state. If the pairing energy is greater than J , then the next electron will go into the d_{z^2} or $d_{x^2-y^2}$ orbitals as an unpaired electron. This situation allows for the most number of unpaired electrons, and it is known as the high spin state. Furthermore, ligands that cause a transition metal to have a small crystal field splitting, which leads to high spin, are called weak-field ligands. Ligands that produce a large crystal field splitting, which leads to low spin, are called strong field ligands.

The splitting energy between the d-orbitals of transition metal affects the magnetic properties of the molecular structures. This phenomenon can be explained by evaluating the superexchange interaction between the transition metal atoms with a ligand atom. Normally, exchange interactions are very short-ranged, confined to electrons in orbitals on the intra-atomic exchange or nearest neighbor atoms but longer-ranged interactions can occur via intermediary atoms and this is termed superexchange. According to that, it can be defined that the superexchange interaction is the interaction of two cations over an intermediate anion. The process of superexchange is a combination of direct exchange and electron transfer. One of the methods which can describe this is Goodenough-Kanamori-Anderson (GKA) rules.

GKA rules are a series of semiempirical rules developed by Goodenough and Kanamori as a refinement to the original model developed by Anderson [31, 30, 29]. This rule is started when two orbitals overlap, both direct exchange and electron transfer can occur. However, if the only direct exchange is generated, it means that there is no overlap between the two orbitals. Therefore, the greater the overlapping wave function, the greater the interaction strength. According to the Pauli exclusion principle, two magnetic cation atoms with half-occupied orbitals which are connected with the non-magnetic anion in the middle, the superexchange interaction will be strongly antiferromagnetic. Beside of that, while the coupling between a cation with a filled orbital and one with a half-filled orbital will be ferromagnetic. The superexchange interaction also depends on the angle between cation-anion-cation atoms. If the angle of cation-anion-cation is 90° , the interaction will be ferromagnetic. If the angle of cation-anion-cation is 180° , the interaction will be antiferromagnetic. Generally, determining the antiferromagnetic and ferromagnetic ground states are generated by various situations as following: when direct exchange and superexchange mechanisms compete with one another; when the cation-anion-cation bond angle deviates away from 180° ; when the electron occupancy of the orbitals is non-static, or dynamical; and when spin-orbit coupling becomes important.

2.6 Thermoelectric Properties Based Anomalous Nernst Effect

Anomalous Nernst effect (ANE) is correlated with anomalous Hall effect (AHE). AHE can occur when there is a combination of magnetic polarization and spin-orbit interaction. This combination will generate Hall voltage although there is no external magnetic field. AHE involves concepts based on topology and geometry. AHE also can be quantized. It acquires quantized value proportional to integer multiples of the conductance quantum which has unit e^2/h . The integer itself is equal to the Chern number which originated from topological properties of material band structures. Quantum AHE is explored in systems which are called Chern insulators.

The intrinsic magnetism contributes to electron group velocity (anomalous velocity). The sum of the anomalous velocity overall occupied band states can be nonzero, involving a contribution to the (anomalous) Hall conductivity σ_{xy} . In other words, the band structure is contributed intrinsically to the σ_{xy} . According to the moderately dirty regime theory [32], when the intrinsic contribution is dominant, σ_{xy} is independent of electrical conductivity. Electrical conductivity itself can be written as

$$\sigma_{xx} = e^2 \tau \sum_n \int v_x^n(k)^2 \left(-\frac{\partial f}{\partial \varepsilon_{nk}} \right) dk. \quad (2.57)$$

In such condition, AHC can be understood in terms of the geometric concepts of the Berry phase and Berry curvature in momentum space which is expressed as

$$\sigma_{xy} = -\frac{e^2}{\hbar} \sum_n \int \Omega_z^n(k) f(\varepsilon_{nk}) dk, \quad (2.58)$$

with Hall ratio is defined by

$$\theta_H = \sigma_{xy} / \sigma_{xx}, \quad (2.59)$$

where e , τ , v_x^n , f , ε_{nk} , \hbar , $\Omega_z^n(k)$, T , k_B and μ are the elementary charge, relaxation time, group velocity of electrons, Fermi-Dirac distribution function, eigen energy, reduced Planck constant, Berry curvature, temperature, Boltzmann's constant, and chemical potential, respectively. The n is the band index and \mathbf{k} is the wave vector. In 2D systems, the intrinsic AHE is quantized in units of e^2/h at temperature $T=0$ when the Fermi level lies between the Bloch state bands. The role of band anti-crossings near the Fermi energy has been identified using first-principles Berry curvature calculations as a mechanism that can lead to a large intrinsic σ_{xy} .

The band decomposition of Berry curvature can be estimated by

$$\mathbf{\Omega}^n(k) \equiv i \langle \nabla_k u_{nk} | \times | \nabla_k u_{nk} \rangle. \quad (2.60)$$

Calculating Berry curvature for each band can be done by using Berry connection defined on discretized Brillouin zone [33]. First, the gauge transformation, Berry curvature $\mathbf{\Omega}^n(k)$ and Berry connection \mathbf{A}_n are defined by

$$U_{\Delta k} = \det \langle u_k^m | u_{k+\Delta k}^l \rangle \quad (2.61)$$

$$\mathbf{A}_n = -i \langle u_{nk} | \partial_k | u_{nk} \rangle = \text{Im} \log U_{\Delta k} \quad (2.62)$$

$$\begin{aligned} \mathbf{\Omega}^n(k) = \nabla \times \mathbf{A}_n = A_{\Delta k_y}(k + \Delta k_x) - A_{\Delta k_y}(k) - (A_{\Delta k_x}(k + \Delta k_y) \\ - A_{\Delta k_x}(k)) + 2\pi n(k) \end{aligned} \quad (2.63)$$

where u_k is normalization wave function and $n(k)$ is lattice Chern number. For the Fermi surface problem, it can be evaluated by fixing the Fermi energy and check the number of eigenvalues smaller than E_F in the gauge transformation $U_{\Delta k}$ which can be denoted by

$$U_{\Delta k} = \det \langle u_k^m | u_{k+\Delta k}^l \rangle (m, l \leq n) \quad (2.64)$$

where n is the maximum number which satisfying $\epsilon_n^k \leq E_F$.

Anomalous Nernst coefficient (ANC) can be determined from the derivative of σ_{xy} as a function of energy. This derivative is called the thermoelectric conductivity tensors which are expressed as

$$\alpha_{ij} = \frac{k_B}{e} \int \sigma_{ij}(\varepsilon) \big|_{T=0} \frac{\varepsilon - \mu}{T} \left(-\frac{\partial f}{\partial \varepsilon}\right) d\varepsilon \quad (2.65)$$

. From Eq. (2.65), the pure Seebeck and Nernst coefficient can be obtained which can be written as

$$S_0 = \frac{\alpha_{xx}}{\sigma_{xx}}, N_0 = \frac{\alpha_{xy}}{\sigma_{xx}}, \quad (2.66)$$

.

The thermoelectric coefficient can be obtained based on the linear response of the charge current, which is given as $j = \sigma_{ij}E + \alpha_{ij}(-\nabla T)$ where E is the electric field, and ∇T is the temperature gradient. The Seebeck and Nernst coefficients are related to the conductivity tensor, and these relationships can be represented as shown below:

$$S = \frac{S_0 + \theta_H N_0}{1 + \theta_H^2}, N = \frac{N_0 - \theta_H S_0}{1 + \theta_H^2}. \quad (2.67)$$

2.7 Computational Scheme

The density functional theory calculation is applied by OpenMX code [25]. The generalized gradient approximation with the Perdew-Burke-Ernzerhof functional is used for treating the exchange-correlation potential [34]. The norm-conserving pseudopotentials and pseudo-atomic localized basis functions are employed. The wave functions are extended by using a linear combination of multiple pseudoatomic orbitals [26]. We specify the pseudoatomic orbitals as Fe6.0S-s2p3d3f1 and Cl7.0-s3p3d2 where 6.0 and 7.0 are the cutoff radius of Fe and Cl atom in the unit Bohr respectively, *S* is soft pseudopotential, and radial function multiplicity of each angular momentum component is defined by the number after *s*, *p*, *d*, *f* in the pseudoatomic orbitals format. We set the charge density cutoff energy at 500.0 Rydbergs and (20,20,1) k-point mesh for the self-consistent field calculations (SCFs). Moreover, the spin-orbit interaction (SOI) was included [35] for the noncollinear density functional calculations. The convergence during k-point sampling and the cut-off energies are checked. We optimized all the atomic positions and lattice parameters of the 1T-FeCl₂ monolayer using the eigenvector-following quasi-Newton algorithm until all the forces were smaller than 10^{-6} Hartrees/Bohr reached [36]. We also determined the lattice constant based on the total energy minimum.

The Wannier90 code was applied to construct maximally localized Wannier functions (MLWFs) based on the results of the DFT calculations for calculating the thermoelectric properties [37]. The 22 Wannier bands are constructed within range of -15 eV to 15 eV for outer window energy and -4 eV to 4 eV for inner window energy. The transport properties based on the MLWFs is computed by using the semiclassical Boltzmann transport theory [38] within constant relaxation time approximation, $\tau=10$ fs, and k-point mesh (300,300,1). This method was used successfully to study the thermoelectric properties of skyrmion crystal and half-Heusler compounds [39, 7, 14].

Chapter 3

Magnetic and Electronic Properties of 1T-FeCl₂ Monolayer

In this chapter, we explore some properties of a 1T-FeCl₂ monolayer. In the atomic structure section, we compare between bulk and monolayer structure. we also compare our calculation with other references to make sure our calculation on the right track. In the magnetic properties section, the magnetic anisotropy energy, superexchange interaction, and Curie temperature are explored. These properties are essential to determine the magnetism in the monolayer system. Next section, the electronic structures are described. we pointed out the relation between band structure and density of states with the octahedral crystal field which will affect the thermoelectric properties of 1T-FeCl₂ monolayer.

3.1 Atomic Structure of 1T-FeCl₂ Monolayer

The side view of the 1T-FeCl₂ monolayer structure can be seen in Fig. 3.1(a) while Fig. 3.1(b) shows the top view of the 1T-FeCl₂ monolayer. Both of the Fig. 3.1(a) and Fig. 3.1(b) show that Fe atom is encircled by six Cl atoms. Those figures also show the hexagonal lattice as the primitive cell of the 1T-FeCl₂ monolayer, wherein the magnitude of the lattice constant (**a**) is equal to that of **b** with the vacuum region $c = 17.26$ Å. The **a** of the 1T-FeCl₂ monolayer was 3.48 Å. The vertical distance between the Cl atoms (d_{Cl-Cl}) is 2.78 Å while the distance between the Fe and Cl atoms (d_{Fe-Cl}) is 2.44 Å. The angle of Fe-Cl-Fe (θ) is 89.90°. These calculated parameters of monolayer were in good agreement with previous theoretical studies on FeCl₂[41, 42, 43, 40]. The calculated lattice constant for monolayer FeCl₂ were similar value to those of bulk FeCl₂, $a=3.6$ Å[45, 44].

According to its atomic structure, the 1T-FeCl₂ monolayer possesses the distorted octahedral crystal field. Four Fe atoms are positioned in a plane, the Cl

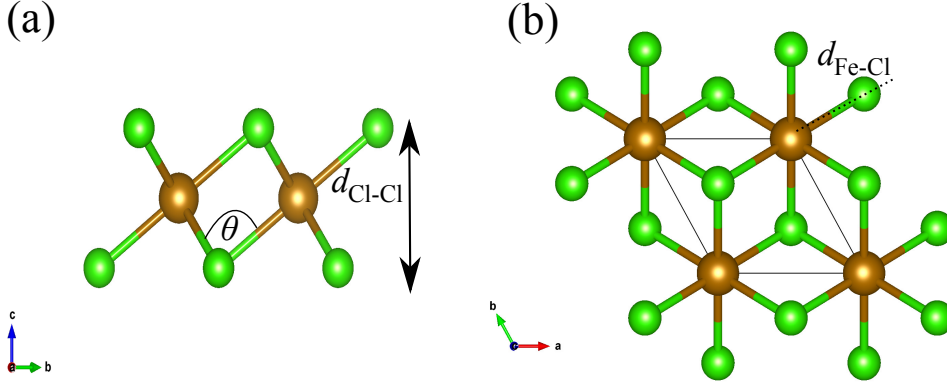


Figure 3.1: (a) Side and (b) top views of 1T-FeCl₂ monolayer structure. Brown and green spheres indicate Fe and Cl atoms, respectively. Structural parameters of 1T-FeCl₂ monolayer, namely, angle between Fe-Cl-Fe atoms, vertical distance of Cl-Cl atoms, and distance between Fe-Cl atom are represented by θ , d_{Cl-Cl} , d_{Fe-Cl} , respectively.

atom is in a symmetrical position just above or below. All spheres can be considered to be hardly filled and touching each other. The six spheres define a regular octahedron, in its interior, there is a defined space for an interstitial atom, bordered by six spheres. This structure will affect the splitting energy which is essential in determining the magnetic and electronic properties.

3.2 Magnetic Properties

The magnetic properties of 1T-FeCl₂ monolayer can be appeared due to magnetic anisotropy energy (MAE). In this research, we calculate MAE based on the different energy between the in-plane and out of plane magnetization of 1T-FeCl₂ monolayer. If the different energy is positive, the ground states are out of plane magnetization. If it is negative, the magnetization will be in-plane. The magnitude from our calculation is 0.05 meV. According to that, MAE of 1T-FeCl₂ monolayer is positive which is out of plane magnetization. The MAE magnitude is originated dominantly from the d-orbital of Fe atom. This result has in good agreement with other results [46].

The next step is to identify the magnetic ordering in 1T-FeCl₂ monolayer. The 2×2 supercell is constructed and the spin ordering has been set to either ferromagnetic (FM) or antiferromagnetic (AFM) as shown in Fig. 3.2(a) and Fig. 3.2(b). We also try another AFM mode but the result remains the same. The exchange energy is calculated based on the different total energy of AFM and FM mode which can be written $E_{EX} = E_{AFM} - E_{FM}$. Positive magnitude indicates that the ground state

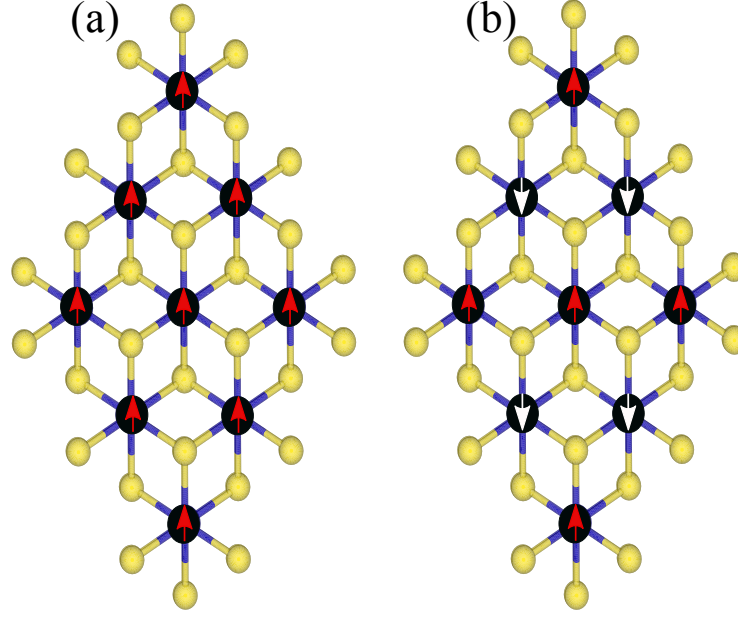


Figure 3.2: Configuration mode for (a) FM and (b) AFM spin arrangements

system is FM. In our calculation, we obtain that the 1T-FeCl₂ monolayer ground states have FM spin ordering. The FM states of 1T-FeCl₂ also can be explained in Goodenough-Kramer-Anderson (GKA) rules [29].

The magnetic properties of 1T-FeCl₂ monolayer can be determined by the competition between the direct exchange interaction of two Fe atoms and the superexchange interaction of Fe-Cl-Fe atoms. The Fe-Cl-Fe superexchange interaction sign can be investigated from the bond angle θ of Fe-Cl-Fe and d orbital configuration. Because θ 1T-FeCl₂ monolayer is 90° , the d orbital of Fe atoms will overlap p orbital of Cl atoms. According to GKA rules, in such bond angles, the superexchange interaction between Fe atoms is deduced only from a potential exchange which is always FM. Beside of that, due to nearly filled d orbital of Fe atoms, the AFM direct exchange interaction between Fe atoms is weakened. It gives rise FM ground states in the 1T-FeCl₂ monolayer.

The transition between paramagnetic (PM) to FM depends on the Curie temperature. There are many methods for calculating the Curie temperature. In our case, we primary use mean-field theory (MFT) [42]. We use the Heisenberg model in which the Hamiltonian can be written as

$$\hat{H} = - \sum_i^j J \hat{m}_i \cdot \hat{m}_j. \quad (3.1)$$

Where J is the Heisenberg exchange energy and $\hat{m}_{i,j}$ is the magnetic moment of

each site in μ_B . The formulation of J in our system is

$$J = \frac{E_{EX}}{12S_{Fe}^2}, \quad (3.2)$$

where S_{Fe} is the high spin magnitude of Fe atoms in the octahedral configuration which has magnitude 2. From that, the Curie temperature in the MFT approximation can be calculated by

$$T_c = \frac{3J}{2k_B}, \quad (3.3)$$

where k_B is Boltzmann constant. We summarized the calculation result in Table 3.1. Most of our calculation parameter results show in good agreement with earlier studies of 1T-FeCl₂ monolayer. However, T_c is slightly different in using Eq. 3.2 although in the same order. This condition is occurred due to the different methods. We use the MFT method while *Kulish et al* use the Monte Carlo simulation method. The magnitude of the Curie temperature is relatively small. However, the Curie temperature can be increased by strain and charge doping [42].

Table 3.1: The atomic and magnetic parameters of 1T-FeCl₂ monolayer which consist of lattice constant a , the angle of Fe-Cl-Fe atoms θ , magnetic anisotropy energy (MAE) E_{MAE} , magnetic moment m , the different energy between FM and AFM E_{EX} , exchange splitting energy J , and Curie temperature T_c

Parameters	Our Calculation	Earlier Studies	References
$a(\text{\AA})$	3.48	3.47	[42]
$\theta(^{\circ})$	91.06	88.80	[46]
E_{MAE}	0.05	0.07	[46]
$m(\mu_B)$	4	4	[42, 41, 46]
E_{EX}	0.371	0.372	[42]
$J(\text{meV})$	7.73	7.75	[42]
$T_c(\text{K})$	134	109	[41]

3.3 Electronic Properties

The electronic band structure of 1T-FeCl₂ monolayer in the FM configuration is shown in the Figure 3.3 (a) and 3.3 (b). It can be seen that the minority states cross the Fermi level, while the majority states have a large gap. It indicates that the ground states of the 1T-FeCl₂ monolayer are half-metallic. These results are in fairly good agreement with those of earlier studies [41, 46].

The bonding mechanism can be explained in the density of states distribution as shown in Fig. 3.3 (c). The distinctive feature of 1T-FeCl₂ monolayer is a significant

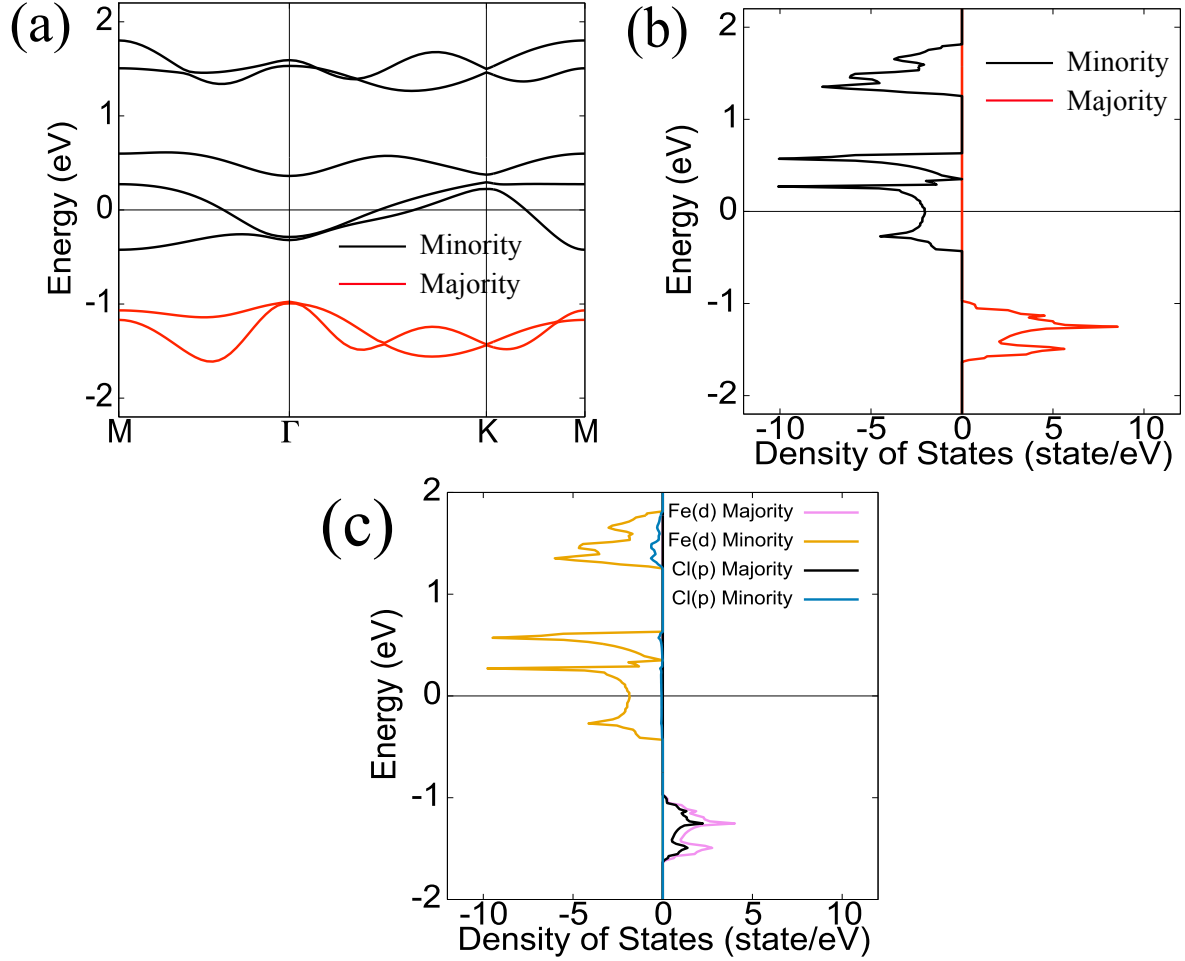


Figure 3.3: The electronic structure of the ferromagnetic 1T-FeCl₂ monolayer, which consists of spin polarized (a) band structure and (b) density of states where red and black lines indicate the majority and minority states, respectively, and (c) the projected density of states (PDOS)

charge transfer. The bonding has a profound ionic character. Cl atoms have a strong affinity for acquiring an extra electron to fill its outer shell. The valence band is formed by Cl atoms 2p bands, while the bottom of the conduction band mainly originates from Fe atom 4s and 3d states. The Fe atom transfers their 4s and 3d electrons to Cl atoms and have a +2 oxidation state; therefore, Fe 4s states are completely unoccupied while 3d orbitals are partly occupied. The spin polarized 3d states of Fe atoms are located within the bandgap. We can observe significant hybridization between Fe atom 3d and Cl atom 2p orbitals.

Most of the states near the Fermi level of the 1T-FeCl₂ monolayer were composed by the 2p orbitals of the Cl atoms and the 3d orbital of the Fe atom, as shown in Fig. 3.3 (c). These states are investigated as anti-bonding states of Fe 3d and Cl 2p. According to the ligand field theory [47], the Cl atoms are weak ligands from the spectroscopic series, therefore 3d Fe atoms in the octahedral field are expected to prefer high spin states. The octahedral geometry of Cl atoms around a Fe atom

leads to the splitting of the energy between the d orbitals. This is identified by electron-electron repulsion between the Fe and Cl orbitals. The e_g ($d_{x^2-y^2}$ and $d_{3z^2-r^2}$) orbitals are directly connected to six Cl atoms so that they have higher Coulombic energy while t_{2g} (d_{xy} , d_{xz} , d_{yz}) orbitals are relatively stable because its position lies between the Cl atoms. The d orbital states, in particular, t_{2g} , will affect the magnitudes of the thermoelectric coefficients of the 1T-FeCl₂ monolayer.

Chapter 4

Thermoelectric Properties of 1T-FeCl₂ Monolayer

In this chapter, we explore the thermoelectric properties based on the anomalous Nernst effect (ANE) of 1T-FeCl₂ monolayer. Anomalous Nernst coefficient(ANC) is related to the pure Seebeck and pure Nernst coefficient. ANC also originated from anomalous Hall conductivity (AHC). The bands near the Fermi level determine the AHC as an intrinsic contribution.

4.1 Anomalous Nernst Coefficient

Table 4.1 shows the thermoelectric properties of the 1T-FeCl₂ monolayer without carrier doping. The main component of N consists of the pure ANC (N_0), the pure Seebeck coefficient (S_0), the Hall angle (θ_H). S_0 contributes to N around 0.2% each. However, since the sign of N_0 and $\theta_H S_0$ are same at both 50 K and 100 K, N_0 , and $\theta_H S_0$ weaken each other. If the chemical potential μ is tuned by carrier doping, N can be increased as can be viewed from the rigid band approximation (RBA) in Fig. 4.1.

Fig. 4.1 describes the chemical potential dependences of the Nernst, N , coefficients of the 1T-FeCl₂ monolayer at 50 K and 100 K . According to it, the value of N is small at $\mu = 0$ at both 50 K and 100 K. Beside of that, a large value N occurs at approximately $\mu = 0.16$ eV, $\mu = 0.31$ eV, and $\mu = 0.35$ eV which denoted by

Table 4.1: Thermoelectric properties of 1T-FeCl₂ monolayer without carrier doping calculated by constant relaxation time, $\tau = 10fs$.

T(K)	$S_0(\mu V/K)$	$N_0(\mu V/K)$	$\theta_H[\times 10^{-2}]$	$N(\mu V/K)$
50	0.46	0.24	0.19	0.24
100	5.51	0.49	0.21	0.48

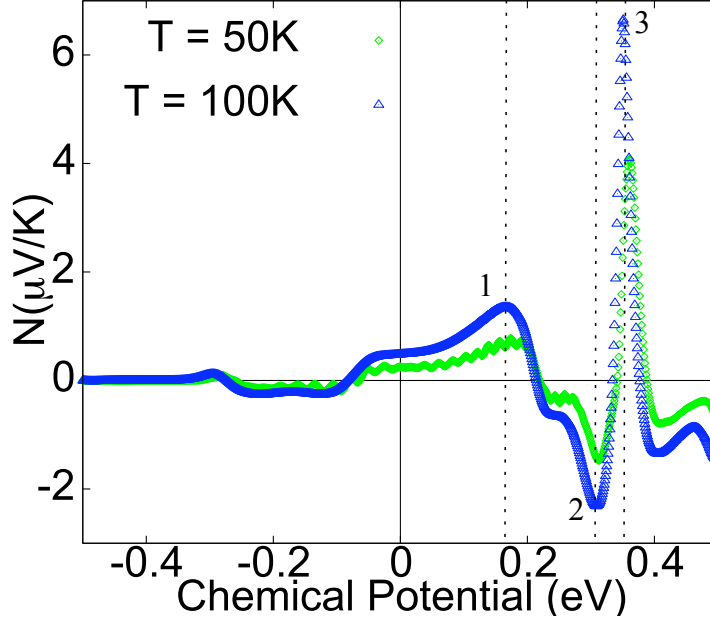


Figure 4.1: Chemical potential and temperature dependence of anomalous Nernst coefficient (ANC), N , at 50 K and 100 K on 1T-FeCl₂ monolayer.

Table 4.2: The peaks of N at chemical potential μ in the Figure 4.1a which is contributed by N_0 , θ_H , and S_0 at 100 K.

Peak	μ	$N_0(\mu\text{V/K})$	θ_H	$S_0(\mu\text{V/K})$	$N(\mu\text{V/K})$
1	0.16	0.62	-0.02	14.2	1.35
2	0.31	-3.96	-0.02	77.2	-2.32
3	0.35	8.13	-0.03	-44.6	6.65

peak 1, 2, and 3, respectively. By using self-consistent field carrier doping methods, the RBA calculation is quite well for 1T-FeCl₂.

The origin of peak 1, 2, and 3 is composed by N_0 and $\theta_H S_0$ in the Fig. 4.2(a) and 4.2(b) respectively. In the peak 1, N_0 and $\theta_H S_0$ have different sig. According to the Eq. (2.67), N_0 and $\theta_H S_0$ will strengthen each other. In Table 4.2, it is demonstrated that S_0 gives 2 % contribution for N which produces N value more than 1 $\mu\text{V/K}$. The different condition is occurred in peak 2 and peak 3. According to Fig. 4.2(a) and 4.2(b), N_0 and $\theta_H S_0$ have same sign which indicate that those variable are weaken each other. However, although the N_0 is decreased, the N is still large as presented in the Table 4.2.

4.2 Anomalous Hall Conductivity

The chemical potential dependence of the AHC (σ_{xy}) and the longitudinal electrical conductivity (σ_{xx}) with $\tau = 10$ fs is exhibited in Fig. 4.3 for elucidating the

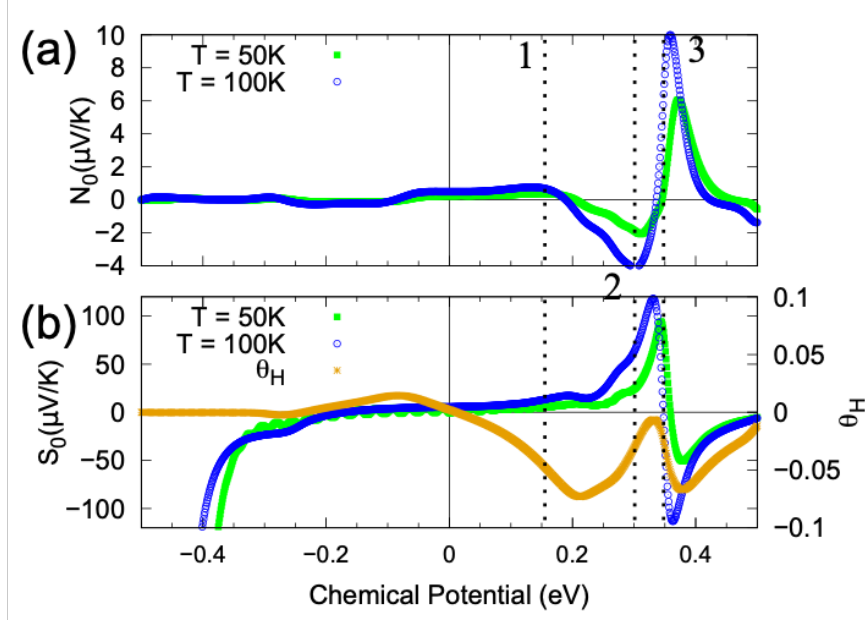


Figure 4.2: Chemical potential and temperature dependence of (a) pure Nernst coefficient, N_0 , and (b) pure Seebeck coefficient, S_0 , at 50 K and 100 K on 1T-FeCl₂ monolayer.

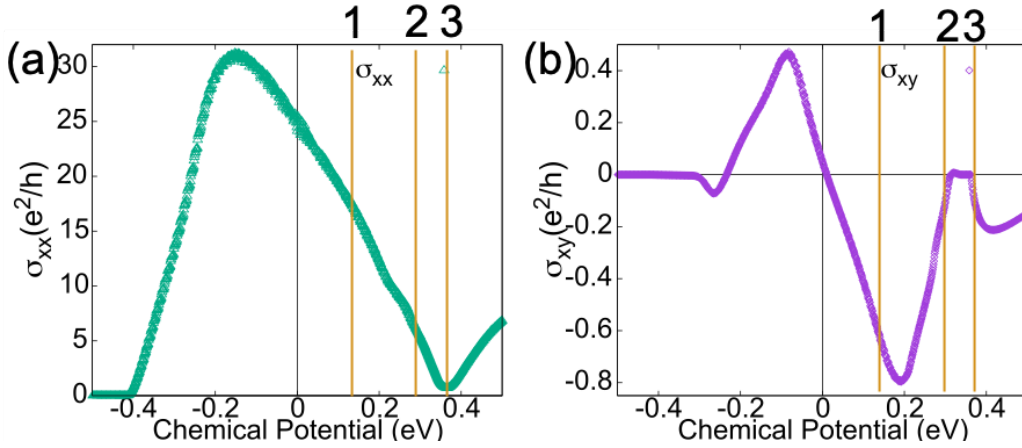


Figure 4.3: Chemical potential and temperature dependence of (a) the AHC (σ_{xy}) and the (b) longitudinal electrical conductivity (σ_{xx}) with $\tau = 10\text{ fs}$ at 0 K.

properties of coefficients N . σ_{xx} as a function of chemical potential influences the magnitude and sign of S_0 . As shown in Fig. 4.3(a), σ_{xx} shows a positive slope at energy values lower than $\varepsilon = -0.2\text{ eV}$, which make S_0 demonstrating a negative value. This is also occurred in the case for N_0 in Fig. 4.3(b). The magnitude and sign of N_0 rely on σ_{xy} as a function of energy. If there is a slope at a energy in $\sigma_{xy}(\varepsilon)$, the N_0 will large around the energy. As stated from Mott's formula, which is $\alpha_{ij} = -\frac{(\pi k_B)^2}{3e} \frac{\partial \sigma_{ij}(\varepsilon)}{\partial \varepsilon} T \big|_{\varepsilon=\mu}$, the N_0 is affected by slope of σ_{xy} . The slope of σ_{xy} on $\mu = -0.3\text{ eV}$ to $\mu = -0.1\text{ eV}$, did not contributes to N_0 because σ_{xx} is large at this point. However, the slope of σ_{xy} around $\mu = -0.1\text{ eV}$ to $\mu = -0.18\text{ eV}$ gives

large contribution for N_0 . Moreover, the large of N around $\mu = 0.3$ eV and $\mu = 0.35$ eV which denoted by peak 2 and 3 as presented on the Figure 4.1 is not mainly originated from σ_{xy} . It is contributed by the σ_{xx} which approaching to zero magnitude.

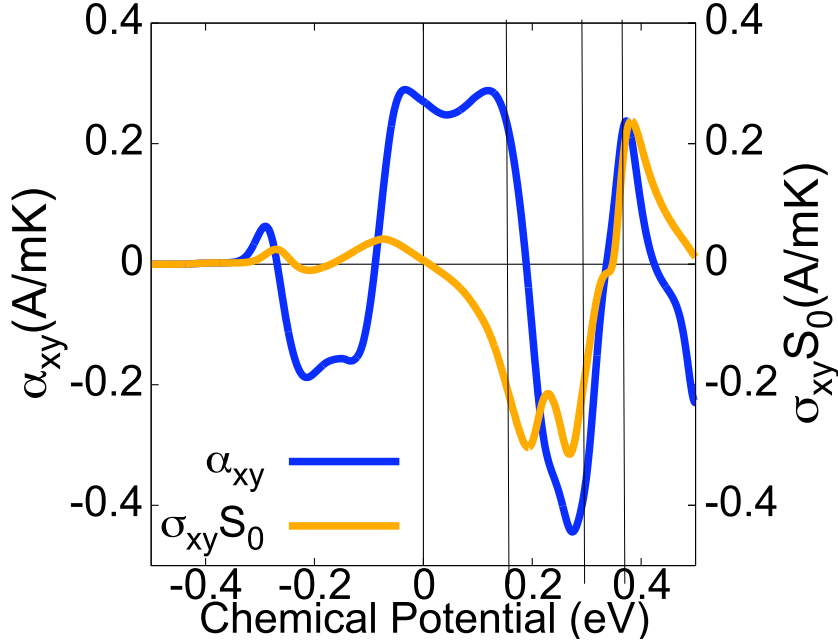


Figure 4.4: Chemical potential dependence of α_{xy} , and $\sigma_{xy} S_0$ at 100 K.

Chemical potential dependence of α_{xy} and $\sigma_{xy} S_0$ at 100 K in the Fig. 4.4 is demonstrated for better understanding the origin of large N in Fig. 4.1. The intrinsic of thermoelectric properties which independent from relaxation time τ is also explained in Fig. 4.4 and it is also accessible in the experiment. It is possible to compare experimental results with theoretical results for the α_{xy} without assuming relaxation time τ [48]. From the Eq. (2.67), the ANC can be expressed as $N = \frac{\alpha_{xy} - \sigma_{xy} S_0}{\gamma}$ where $\gamma = (1 + \theta_H^2) \sigma_{xx}$. According to the Fig. 4.4, the different sign of α_{xy} and $\sigma_{xy} S_0$ give contribution to peak 1 which shown in Fig. 4.1(a). In the α_{xy} and $\sigma_{xy} S_0$ at chemical potential, peak 2 and peak 3 have same sign and almost same magnitude. Corresponding to this condition, α_{xy} and $\sigma_{xy} S_0$ are reduced each other which will cause that N should be approached zero at these chemical potential. However, because of band gap around chemical potential in those peaks, σ_{xx} becomes small which lead to generate peak 2 and peak 3 in Fig. 4.1. In addition, α_{xy} is tend to stable between $\mu = 0.04$ eV to $\mu = 0.16$ eV. It is generated from a large slope of σ_{xy} in Fig. 4.1(b). This result match with Mott's relation. It also illustrated that the large N can be achieved without the change of α_{xy} . Beside of that, although their electronic structures are different, α_{xy} of 1T-FeCl₂ monolayer is almost same with Fe₃GeTe₂ (FGT)[49]. FGT has thermoelectric conductivity $\alpha_{xy} = 0.3$ A/mK and large Hall ratio $\theta_H = 0.07$ while as shown the Fig.4.2(b) and Fig.4.4, 1T-FeCl₂

monolayer possess $\theta_H = 0.072$ and $\alpha_{xy} = 0.35$ A/mK.

4.3 Band Contribution to Anomalous Hall Conductivity

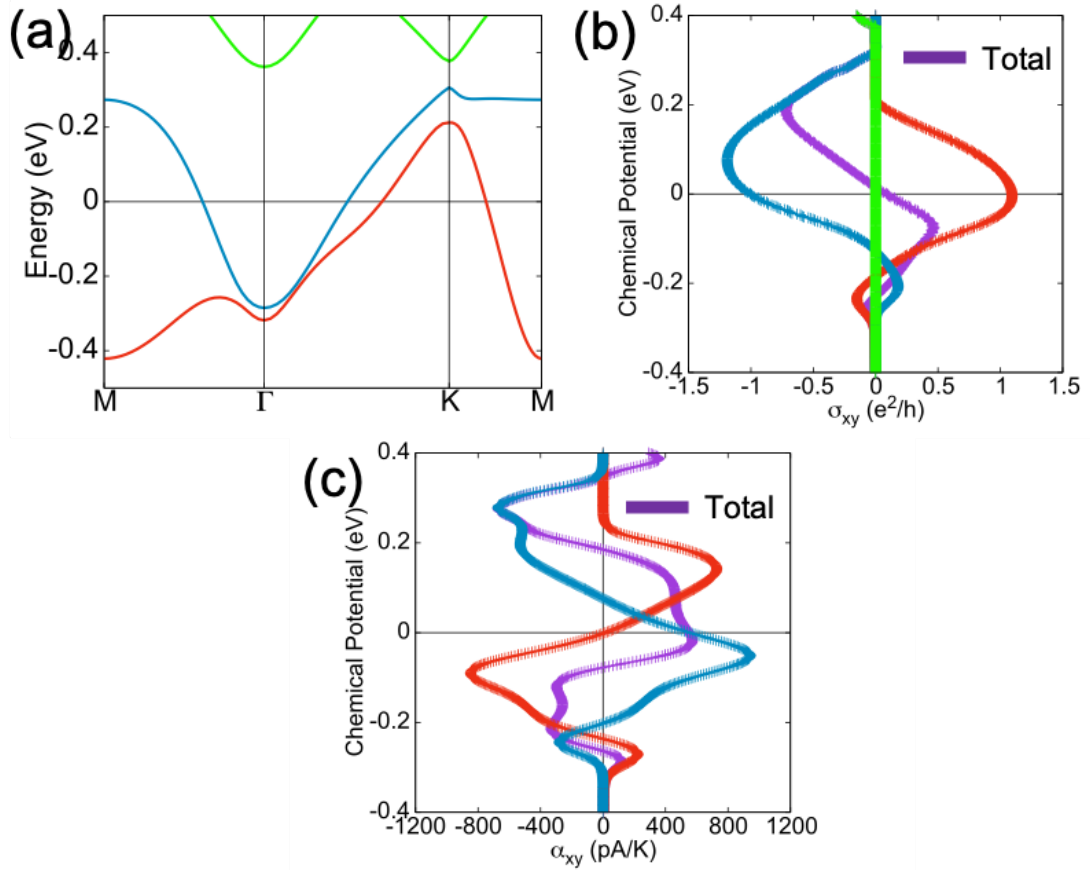


Figure 4.5: (a) Band structure with SOI, band decomposition in the chemical potential dependence of (b) σ_{xy} and (c) α_{xy} of 1T-FeCl₂ monolayer. Red, blue, and green lines indicate the band contribution near Fermi level.

Next, we will investigate the origin of σ_{xy} peaks which lead to large N . Fig. 4.5(a) demonstrates the band structure with SOI. The σ_{xy} sign change can be associated with the band filling near the Fermi level. In Fig. 4.5(a), the red band is about 1/4 filling, the blue band is about 3/4 filling and the green band is no filling due to lies in the conduction band. If the charge doping is given, it will alter the charge filling near Fermi level between the red and blue band and the Fermi level will be shifted. The band filling effect on σ_{xy} is presented in Fig. 4.5(b). The red band has a positive sign of σ_{xy} and the blue band has a negative sign of σ_{xy} while the green band has zero magnitudes which indicate that the band does not give a contribution to σ_{xy} near Fermi level. The total σ_{xy} which marked by purple lines is contributed

by the sum of the red and blue band. The α_{xy} is displayed in Fig. 4.5(c). The α_{xy} which is described by the purple line in Fig. 4.1d near Fermi level is generated by the slope of the red and blue band at the chemical potential. Beside of that, because there is no slope, the green band does not give any contribution to α_{xy} . According to Fig. Fig. 4.5(a), it is found that the peak of σ_{xy} occurred at $\mu \sim 0.2$ eV. There is possibility to obtain large Berry curvature in this chemical potential based on Eq. (2.58).

The origin of red and blue band contribution also can be elucidated in the Berry curvature as presented in Fig. 4.5. The detailed interpretation of Berry curvature which is associated with the blue and red band is demonstrated in Fig. 4.5(a). Berry curvatures in the Γ -K line have a value which is composed of the red and blue band. These magnitudes are generated because mirror symmetry is broken in Γ -K line that resulting unusual SOI which called Ising SOI [52, 50, 51]. The origin of Ising SOI comes from d -orbitals of a transition metal which rising large Berry curvature in Γ -K line. However, Berry curvatures of the blue and red bands on the Γ -K line around Γ -point cancel each other while it strengthens around the K-point. The sign difference of the Berry curvature also affects σ_{xy} . The blue band leads to σ_{xy} exhibiting a negative peak while the red band generates a positive peak of σ_{xy} . Beside of that, the large summation of Berry curvature is exposed around K-point in the Brillouin zone at $\mu \sim 0.2$ eV in Fig. 4.5(b). These facts indicate that the σ_{xy} origin can be attributed to the Berry curvature around K-point mentioned above.

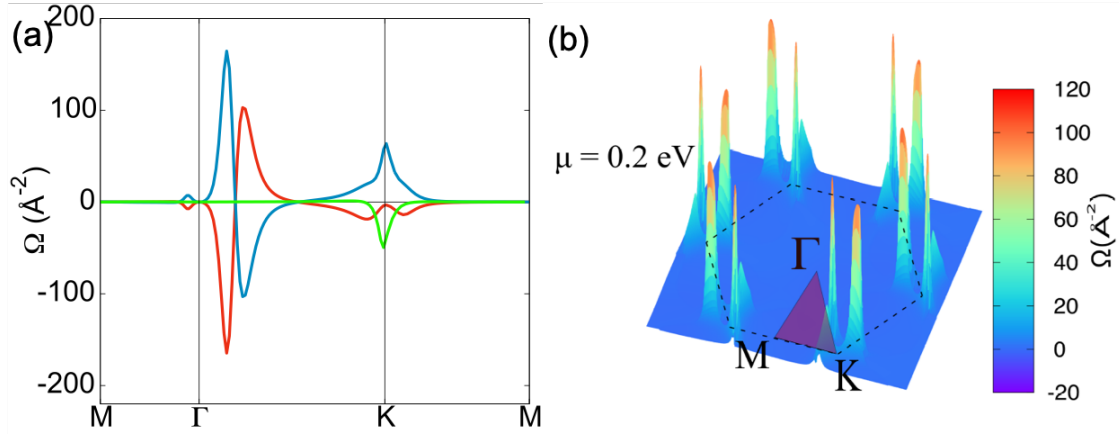


Figure 4.6: The chemical potential dependence of (a) Berry curvature summation at $\mu \sim 0.2$ eV, and (b) Berry curvature from band decomposition of 1T-FeCl₂ monolayer. Red, blue, and green lines indicate the band contribution near Fermi level.

Chapter 5

Conclusion

5.1 Summary

The density functional calculations were performed for 1T-FeCl₂ monolayer. The atomic structure of 1T-FeCl₂ monolayer is formed by a hexagonal lattice primitive cell. Because Fe atom lies in the plane and its position above and below is surrounded by Cl atoms, the distorted octahedral crystal field is constructed. The octahedral crystal field affects the magnetic and electronic properties of a 1T-FeCl₂ monolayer. In the magnetic case, the ferromagnetic becomes ground states of 1T-FeCl₂ monolayer because the angle between Fe-Cl-Fe atoms is 90 ° which gives the ferromagnetic superexchange interaction dominant compared with antiferromagnetic direct exchange interaction. In the electronic properties, the half-metal characteristics are obtained because there is large splitting in the d orbital of Fe atom as consequences of Coloumb interaction with p orbital of Cl atoms.

There are two origins of large anomalous Nernst coefficient (ANC) which can be reached in the 1T-FeCl₂ monolayer based on the rigid band approximation (RBA). First, the ANC is reinforced by the pure Nernst and Seebeck coefficient. In this case, the slope of anomalous Hall conductivity gives a significant contribution to ANC. Second, the large ANC comes from the near-zero electrical conductivity although the pure Nernst and Seebeck coefficient are weakened each other. The maximum magnitude of ANC has a value as high as 6.65 $\mu\text{V}/\text{K}$ for chemical potentials of 0.33 eV to 0.36 eV based on rigid band approximation (RBA). The high value of the ANC can be attributed to the large Berry curvature, which is induced by the bands around the K-point of the Brillouin zone of the 1T-FeCl₂ monolayer. These results suggest that the ferromagnetic half-metallic 1T-FeCl₂ monolayer possesses high ANC magnitudes which can potentially be applied in thermoelectric devices.

Table 5.1: The 2D magnetic materials which experimentally discovered

2D Magnetic Material	References
Fe_3GeTe_2 (FGT)	[54]
$\text{Cr}_2\text{Ge}_2\text{Te}_6$ (CGT)	[17]
CrI_3	[16]
VSe_2	[55]

5.2 Future Scope

The anomalous Nernst effect of 1T- FeCl_2 monolayer has not experimentally explored yet although its layered structures have been recently discovered [53]. In the density functional calculation, several cases can be evaluated and challenged. The challenge in the 1T- FeCl_2 is the vacuum region which in the calculation, it can affect the thermoelectric conductivity tensors as same as Chern number. It is required some explanation of how to choose the vacuum region in the slab calculation which matches the experimental case. Second, the relaxation time calculation is required for a better explanation of anomalous Nernst coefficient. In the magnetic material cases, the magnon and electron interaction should be included in the relaxation time calculation. Beside of that, the RBA calculation can be proved with charge doping self-consistent field with using supercell size. It also can be cleared about the required charge doping concentration.

Another 2D magnetic material that has been found experimentally can potentially possess the large anomalous Nernst effect which can be seen in Table 5.1. The anomalous Nernst coefficient calculation of those materials will be performed in the future. In the FGT case, the anomalous Nernst effect has been discovered. It is obtained that the $\alpha_{xy} = 0.3$ A/mk. However, we believe that α_{xy} depends on the vacuum region (sample thickness). So, the layer dependent calculation in the 2D magnetic material will be important to investigate. Furthermore, the CGT has a high Seebeck coefficient [56]. This large magnitude has the possibility to be coupled with a pure Nernst coefficient which affects the large anomalous Nernst coefficient. This advantage also can be occurred in the CrI_3 due to the same insulator characteristics. Lastly, the VSe_2 can be the candidate for thermoelectric based anomalous Nernst effect because its Curie temperature exceeds the room temperature. In other words, the study of anomalous Nernst effect of VSe_2 monolayer is clearly visible in the experiment.

Bibliography

- [1] Yuya Sakuraba. “Potential of thermoelectric power generation using anomalous Nernst effect in magnetic materials”. In: *Scr. Mater.* 111 (2016), pp. 29–32.
- [2] TC Harman and JM Honig. “Theory of galvano-thermomagnetic energy conversion devices. II. Refrigerators and heat pumps”. In: *J. Appl. Phys.* 33 (1962), pp. 3188–3194.
- [3] Shinji Isogami, Koki Takanashi, and Masaki Mizuguchi. “Dependence of anomalous Nernst effect on crystal orientation in highly ordered γ -Fe₄N films with anti-perovskite structure”. In: *Applied Physics Express* 10.7 (2017), p. 073005.
- [4] Tsao-Chi Chuang et al. “Enhancement of the anomalous Nernst effect in ferromagnetic thin films”. In: *Physical Review B* 96.17 (2017), p. 174406.
- [5] K Hasegawa et al. “Material dependence of anomalous Nernst effect in perpendicularly magnetized ordered-alloy thin films”. In: *Applied Physics Letters* 106.25 (2015), p. 252405.
- [6] Yo Pierre Mizuta and Fumiyuki Ishii. “Contribution of Berry curvature to thermoelectric effects”. In: *Proceedings of the International Conference on Strongly Correlated Electron Systems (SCES2013)*. 2014, p. 017035.
- [7] Yo Pierre Mizuta and Fumiyuki Ishii. “Large anomalous Nernst effect in a skyrmion crystal”. In: *Sci. Rep.* 6 (2016), p. 28076.
- [8] Robert Karplus and JM Luttinger. “Hall effect in ferromagnetics”. In: *Phys. Rev.* 95.5 (1954), p. 1154.
- [9] Jan Smit. “Physica (Amsterdam) 21, 877 (1955)”. In: *Phys. Rev. B* 8 (1973), p. 2349.
- [10] Arup Ghosh, Rajasree Das, and Ramanathan Mahendiran. “Skew scattering dominated anomalous Nernst effect in $\text{La}_{1-x}\text{Na}_x\text{MnO}_3$ ”. In: *J. Appl. Phys.* 125.15 (2019), p. 153902.
- [11] Xiaokang Li et al. “Anomalous Nernst and Righi-Leduc effects in Mn_3Sn : Berry curvature and entropy flow”. In: *Phys. Rev. Lett.* 119.5 (2017), p. 056601.

- [12] Muhammad Ikhlas et al. “Large anomalous Nernst effect at room temperature in a chiral antiferromagnet”. In: *Nat. Phys.* 13.11 (2017), pp. 1085–1090.
- [13] Di Xiao, Ming-Che Chang, and Qian Niu. “Berry phase effects on electronic properties”. In: *Rev. Mod. Phys.* 82.3 (2010), p. 1959.
- [14] Yo Pierre Mizuta, Hikaru Sawahata, and Fumiyuki Ishii. “Large anomalous Nernst coefficient in an oxide skyrmion crystal Chern insulator”. In: *Phys. Rev. B* 98 (2018), p. 205125.
- [15] Cui-Zu Chang et al. “Experimental observation of the quantum anomalous Hall effect in a magnetic topological insulator”. In: *Science* 340 (2013), pp. 167–170.
- [16] Bevin Huang et al. “Layer-dependent ferromagnetism in a van der Waals crystal down to the monolayer limit”. In: *Nature* 546 (2017), p. 270.
- [17] Cheng Gong et al. “Discovery of intrinsic ferromagnetism in two-dimensional van der Waals crystals”. In: *Nature* 546 (2017), p. 265.
- [18] Roman Anufriev, Jeremie Maire, and Masahiro Nomura. “Reduction of thermal conductivity by surface scattering of phonons in periodic silicon nanostructures”. In: *Phys. Rev. B* 93 (2016), p. 045411.
- [19] Kostya S Novoselov et al. “Two-dimensional gas of massless Dirac fermions in graphene”. In: *Nature* 438 (2005), p. 197.
- [20] LD Hicks and Mildred S Dresselhaus. “Effect of quantum-well structures on the thermoelectric figure of merit”. In: *Phys. Rev. B* 47 (1993), p. 12727.
- [21] Myoung-Jae Lee et al. “Thermoelectric materials by using two-dimensional materials with negative correlation between electrical and thermal conductivity”. In: *Nat. Commun.* 7 (2016), p. 12011.
- [22] Hiromichi Ohta et al. “Giant thermoelectric Seebeck coefficient of a two-dimensional electron gas in SrTiO_3 ”. In: *Nat. Mater.* 6 (2007), p. 129.
- [23] Pierre Hohenberg and Walter Kohn. “Inhomogeneous electron gas”. In: *Physical review* 136.3B (1964), B864.
- [24] Walter Kohn and Lu Jeu Sham. “Self-consistent equations including exchange and correlation effects”. In: *Physical review* 140.4A (1965), A1133.
- [25] Taisuke Ozaki et al. “www.openmx-square.org”. In: ().
- [26] T. Ozaki. “Variationally optimized atomic orbitals for large-scale electronic structures”. In: *Phys. Rev. B* 67 (15 Apr. 2003), p. 155108.
- [27] Nicola Marzari and David Vanderbilt. “Maximally localized generalized Wannier functions for composite energy bands”. In: *Physical review B* 56.20 (1997), p. 12847.

- [28] Claude A Daul. “Ligand Field Theory: An ever-modern theory”. In: *Journal of Physics: Conference Series*. Vol. 428. 1. IOP Publishing. 2013, p. 012023.
- [29] John B Goodenough. “An interpretation of the magnetic properties of the perovskite-type mixed crystals $\text{La}_{1-x}\text{Sr}_x\text{CoO}_{3-\lambda}$ ”. In: *Journal of Physics and chemistry of Solids* 6.2-3 (1958), pp. 287–297.
- [30] Junjiro Kanamori. “Superexchange interaction and symmetry properties of electron orbitals”. In: *Journal of Physics and Chemistry of Solids* 10.2-3 (1959), pp. 87–98.
- [31] Philip W Anderson. “Theory of magnetic exchange interactions: exchange in insulators and semiconductors”. In: *Solid state physics*. Vol. 14. Elsevier, 1963, pp. 99–214.
- [32] Shigeki Onoda, Naoyuki Sugimoto, and Naoto Nagaosa. “Quantum transport theory of anomalous electric, thermoelectric, and thermal Hall effects in ferromagnets”. In: *Phys. Rev. B* 77.16 (2008), p. 165103.
- [33] Takahiro Fukui, Yasuhiro Hatsugai, and Hiroshi Suzuki. “Chern Numbers in Discretized Brillouin Zone: Efficient Method of Computing (Spin) Hall Conductances”. In: *J. Phys. Soc. Jpn.* 74 (2005), pp. 1674–1677.
- [34] John P. Perdew, Kieron Burke, and Matthias Ernzerhof. “Generalized Gradient Approximation Made Simple”. In: *Phys. Rev. Lett.* 77 (18 Oct. 1996), pp. 3865–3868.
- [35] Gerhard Theurich and Nicola A Hill. “Self-consistent treatment of spin-orbit coupling in solids using relativistic fully separable ab initio pseudopotentials”. In: *Phys. Rev. B* 64 (2001), p. 073106.
- [36] Jon Baker. “An algorithm for the location of transition states”. In: *J. Comput. Chem.* 7 (1986), pp. 385–395.
- [37] Arash A Mostofi et al. “An updated version of wannier90: A tool for obtaining maximally-localised Wannier functions”. In: *Comp Phys. Comm.* 185.8 (2014), pp. 2309–2310.
- [38] John M Ziman. *Principles of the Theory of Solids*. Cambridge university press, 1979.
- [39] Susumu Minami et al. “First-principles study on thermoelectric properties of half-Heusler compounds CoMSb ($\text{M} = \text{Sc}, \text{Ti}, \text{V}, \text{Cr}, \text{and Mn}$)”. In: *Appl. Phys. Lett.* 113 (2018), p. 032403.
- [40] Yulin Feng et al. “Robust half-metallicities and perfect spin transport properties in 2D transition metal dichlorides”. In: *J. Mater. Chem. C* 6.15 (2018), pp. 4087–4094.

- [41] Vadym V. Kulish and Wei Huang. “Single-layer metal halides MX_2 ($\text{X} = \text{Cl}, \text{Br}, \text{I}$): stability and tunable magnetism from first principles and Monte Carlo simulations”. In: *J. Mater. Chem. C* 5 (2017), pp. 8734–8741.
- [42] Engin Torun et al. “Stable half-metallic monolayers of FeCl_2 ”. In: *Appl. Phys. Lett.* 106 (2015), p. 192404.
- [43] Sherin A Saraireh and Mohammednoor Altarawneh. “Thermodynamic stability and structures of iron chloride surfaces: A first-principles investigation”. In: *J. Chem. Phys.* 141 (2014), p. 054709.
- [44] MK Wilkinson et al. “Neutron Diffraction Investigations of the Magnetic Ordering in FeBr_2 , CoBr_2 , FeCl_2 , and CoCl_2 ”. In: *Phys. Rev.* 113 (1959), p. 497.
- [45] C Vettier and WB Yelon. “The structure of FeCl_2 at high pressures”. In: *J. Phys. Chem. Solids* 36 (1975), pp. 401–405.
- [46] Huiling Zheng et al. “Enhancing the perpendicular magnetic anisotropy of 1T- FeCl_2 monolayer by applying strain: first-principles study”. In: *J. Magn. Magn. Mater.* 444 (2017), pp. 184–189.
- [47] F. Albert Cotton. “I - Ligand field theory”. In: *J. Chem. Educ.* 41 (1964), p. 466.
- [48] Akito Sakai et al. “Giant anomalous Nernst effect and quantum-critical scaling in a ferromagnetic semimetal”. In: *Nat. Phys.* 14.11 (2018), p. 1119.
- [49] Jinsong Xu, W Adam Phelan, and Chia-Ling Chien. “Large anomalous Nernst effect in a van der Waals ferromagnet Fe_3GeTe_2 ”. In: *Nano Lett.* 19.11 (2019), pp. 8250–8254.
- [50] Girish Sharma. “Tunable topological Nernst effect in two-dimensional transition-metal dichalcogenides”. In: *Phys. Rev. B* 98 (7 Aug. 2018), p. 075416.
- [51] E. Cappelluti et al. “Tight-binding model and direct-gap/indirect-gap transition in single-layer and multilayer MoS_2 ”. In: *Phys. Rev. B* 88 (7 Aug. 2013), p. 075409.
- [52] Z. Y. Zhu, Y. C. Cheng, and U. Schwingenschlogl. “Giant spin-orbit-induced spin splitting in two-dimensional transition-metal dichalcogenide semiconductors”. In: *Phys. Rev. B* 84 (15 Oct. 2011), p. 153402.
- [53] Xuhan Zhou et al. “Atomically Thin 1T- FeCl_2 Grown by Molecular-Beam Epitaxy”. In: *The Journal of Physical Chemistry C* 124.17 (2020), pp. 9416–9423.
- [54] Zaiyao Fei et al. “Two-dimensional itinerant ferromagnetism in atomically thin Fe_3GeTe_2 ”. In: *Nature materials* 17.9 (2018), pp. 778–782.

- [55] Zhong-Liu Liu et al. “Epitaxially grown monolayer VSe₂: an air-stable magnetic two-dimensional material with low work function at edges”. In: *Science Bulletin* 63.7 (2018), pp. 419–425.
- [56] Dingfeng Yang et al. “Cr₂Ge₂Te₆: high thermoelectric performance from layered structure with high symmetry”. In: *Chemistry of Materials* 28.6 (2016), pp. 1611–1615.